



Sensitivity to triple Higgs couplings via di-Higgs production in the 2HDM at the (HL-)LHC

F. Arco^{1,2,a}, S. Heinemeyer^{2,b}, M. Mühlleitner^{3,c}, K. Radchenko^{4,d}

¹ Departamento de Física Teórica, Universidad Autónoma de Madrid, Cantoblanco, 28049 Madrid, Spain

² Instituto de Física Teórica (UAM/CSIC), Universidad Autónoma de Madrid, Cantoblanco, 28049 Madrid, Spain

³ Institute for Theoretical Physics, Karlsruhe Institute of Technology, 76128 Karlsruhe, Germany

⁴ Deutsches Elektronen-Synchrotron DESY, Notkestr. 85, 22607 Hamburg, Germany

Received: 31 July 2023 / Accepted: 27 October 2023
© The Author(s) 2023

Abstract An important task of the LHC is the investigation of the Higgs-boson sector. Of particular interest is the reconstruction of the Higgs potential, i.e. the measurement of the Higgs self-couplings. Based on previous analyses, within the 2-Higgs-Doublet Model (2HDM) type I, we analyze several two-dimensional benchmark planes that are over large parts in agreement with all theoretical and experimental constraints. For these planes we evaluate di-Higgs production cross sections at the (HL-)LHC with a center-of-mass energy of 14 TeV at next-to-leading order in the heavy top-quark limit with the code HPAIR. We investigate in particular the process $gg \rightarrow hh$, with h being the Higgs boson discovered at the LHC with a mass of about 125 GeV. The top box diagram of the loop-mediated gluon fusion process into Higgs pairs interferes with the s -channel exchange of the two \mathcal{CP} -even 2HDM Higgs bosons h and H . The latter two involve the triple Higgs couplings (THCs) λ_{hhh} and λ_{hhH} , respectively, possibly making them accessible at the HL-LHC. Depending on the size of the involved top-Yukawa and THCs as well as on the mass of H , the contribution of the s -channel H diagram can be dominating or be highly suppressed. We find regions of the allowed parameter space in which the di-Higgs production cross section can differ by many standard deviations from its SM prediction, indicating possible access to deviations in λ_{hhh} from the SM value λ_{SM} and/or contributions involving λ_{hhH} . The sensitivity to the beyond-the-SM (BSM) THC λ_{hhH} is further analyzed employing the m_{hh} distributions. We demonstrate how a possible measurement of λ_{hhH} depends on the various experimental uncertainties.

Depending on the underlying parameter space, the HL-LHC may have the option not only to detect BSM THCs, but also to provide a first rough measurement of their sizes.

1 Introduction

The discovery of a new scalar particle with a mass of ~ 125 GeV by ATLAS and CMS [1–3] – within the experimental and theoretical uncertainties – is in agreement with the properties of the Standard Model (SM) Higgs boson. On the other hand, no conclusive sign of Higgs bosons beyond the SM (BSM) has been observed so far. However, the experimental results about the state at ~ 125 GeV, whose couplings are known up to now to an experimental precision of roughly ~ 10 – 20% , leave ample room for interpretations in BSM models. Many BSM models feature extended Higgs-boson sectors with correspondingly extended Higgs potentials. Consequently, one of the main tasks of present and future colliders will be to determine whether the observed scalar boson forms part of the Higgs sector of an extended model, or not.

In contrast to the Higgs couplings to the SM 3rd generation fermions and gauge bosons, the trilinear Higgs self-coupling λ_{hhh} remains to be determined. So far it has been constrained by ATLAS [4] to be inside the range $-0.4 < \lambda_{hhh}/\lambda_{SM} < 6.3$ at the 95% CL and $-1.24 < \lambda_{hhh}/\lambda_{SM} < 6.49$ at the 95% CL by CMS [5], both assuming a SM-like top-Yukawa coupling of the light Higgs. Many BSM models can still induce significant deviations in the trilinear coupling λ_{hhh} of the SM-like Higgs boson with respect to the SM value, see, e.g., Ref. [6] for an up-to-date investigation. For recent reviews on the measurement of the triple Higgs couplings at future colliders see for instance Refs. [7, 8]. In case a BSM

^a e-mail: Francisco.Arco@uam.es

^b e-mail: Sven.Heinemeyer@cern.ch (corresponding author)

^c e-mail: margarete.muehlleitner@kit.edu

^d e-mail: kateryna.radchenko@desy.de

Higgs sector manifests itself, it will be a prime task to measure also the BSM trilinear Higgs self-couplings. Despite the relevance of the topic, the prospects of measuring BSM values of λ_{hhh} and possibly other BSM triple Higgs couplings (THCs), taking into account the experimental environment of the (HL-)LHC have not been investigated in the literature so far.

One of the simplest extensions of the SM Higgs sector is the 2-Higgs-Doublet Model (2HDM) [9–12], where a second Higgs doublet is added to the SM Higgs sector, leading to five physical Higgs bosons. To avoid flavor-changing neutral currents at tree level, a \mathbb{Z}_2 symmetry is imposed [13]. Depending on how this symmetry is extended to the fermion sector, four types of the 2HDM can be realized, we only analyze Type I, in which only one of the doublets couples to all the fermions and gauge bosons.

In Ref. [14] an analysis was presented of the possible size of THCs in the 2HDM type I and II taking into account all relevant experimental and theoretical constraints.¹ For that analysis it was assumed that the lightest \mathcal{CP} -even Higgs-boson h is SM-like with a mass of $m_h \sim 125$ GeV. All other Higgs bosons were assumed to be heavier. (An update and extension to type III and IV was presented in Ref. [15].) Future e^+e^- linear colliders, like the ILC [16] and CLIC [17], will play a key role for the measurement of the Higgs potential and in detecting possible deviations from the SM with high precision [7, 8, 18–21].² Employing the results of Ref. [14], in Ref. [22] the sensitivity of the ILC and CLIC to various 2HDM THCs (including BSM THCs) was analyzed. Further analyses of THCs at e^+e^- colliders were presented in Refs. [23, 24]. Corresponding analyses of the (HL-)LHC sensitivity to BSM THCs, however, are missing so far. Recent reviews on triple Higgs couplings at e^+e^- colliders can be found in Refs. [7, 8, 20, 21].

In this paper, based on the results of Ref. [14], we complement the above results with an analysis of the sensitivity to BSM triple Higgs couplings at the LHC, and in particular its high-luminosity phase, the HL-LHC. Further analyses involving BSM triple Higgs couplings can be found in Refs. [6, 8, 25–27]. However, while these papers took the effects of BSM THCs into account, to our knowledge no analysis for the (HL-)LHC exists attempting the investigation presented in this paper: to quantify the potential sensitivity to BSM triple Higgs couplings.

The main Higgs pair production process at the LHC is gluon fusion into Higgs pairs [28]. Here we investigate in particular $gg \rightarrow hh$ in the 2HDM type I, with h corresponding to the state discovered at the LHC at ~ 125 GeV. The process is loop-mediated already at leading order and consists of a triangle and a box top-loop contribution. In the SM, the box diagram interferes destructively with the triangle contribution. In the 2HDM, an exchange of both h and H in the s -channel are possible. A resonantly produced H with subsequent decay into hh can lead to a significantly enhanced cross section. For our analysis, we take into account the next-to-leading order QCD corrections to the process in the heavy top-quark limit [29] by making use of the accordingly modified [6, 30] program HPAIR. In the first part of our analysis, focusing on the effects of THCs on the total di-Higgs production cross section, we find regions of the allowed parameter space in which the di-Higgs production cross section can differ by several standard deviations from its SM prediction, indicating possible access to deviations in λ_{hhh} from λ_{SM} and/or contributions involving λ_{hhH} . This demonstrates the general possibility to have sensitivity to λ_{hhh} and λ_{hhH} at the HL-LHC. In the second step of our analysis, the sensitivity to λ_{hhH} is further analyzed employing the m_{hh} distributions in the $gg \rightarrow hh$ production cross section. We investigate for the first time how a possible measurement of λ_{hhH} depends on the assumed experimental uncertainties in m_{hh} , such as smearing, bin width, as well as on the position of the bins. Our findings clearly indicate where experimental analyses should be improved to gain access to BSM THCs. We demonstrate that, depending on the underlying parameter space, the HL-LHC may have the potential not only to detect BSM triple Higgs couplings, but also to provide a first rough measurement of their size.

Our paper is organized as follows. In Sect. 2 we briefly review the 2HDM, fix our notation, define the benchmark planes (representing the phenomenological variations of the 2HDM parameter space) used later for our investigation and summarize the constraints that we apply (which are the same as in Refs. [14, 15]). As a requisite for our analysis, the di-Higgs production cross sections in the benchmark planes are presented in Sect. 3 and analyzed w.r.t. their dependence on the triple Higgs couplings in the contribution from the s -channel H exchange. In the first step of our analysis, in Sect. 3.3 we analyze a possible sensitivity of the di-Higgs production cross section at the (HL-)LHC to λ_{hhh} and in particular to λ_{hhH} . Finally, as the second step in our analysis in Sect. 4 we present the possible HL-LHC sensitivity to λ_{hhH} via the m_{hh} distribution, and in Sect. 5 also assess its dependence on smearing, bin width and position of the bins. Our conclusions are given in Sect. 6.

¹ For an analysis of THCs in the \mathcal{CP} -conserving and \mathcal{CP} -violating 2HDM, the Next-to-2HDM and the Next-to-Minimal Supersymmetric extension of the SM (NMSSM), see Ref. [6], where in addition the constraints from Higgs pair production measurements at the LHC were taken into account.

² Circular colliders such as FCC-ee or CEPC have only very limited sensitivity to the SM-like THC via loop effects in single Higgs production.

2 The model and the constraints

In this section we give a short description of the 2HDM to fix our notation. We briefly review the theoretical and experimental constraints, which are taken over from Refs. [14, 15]. Finally we will define the benchmark planes for our analysis of the $gg \rightarrow hh$ production cross section.

2.1 The 2HDM

We assume the \mathcal{CP} -conserving 2HDM [9–12], where the potential can be written as,

$$V = m_{11}^2(\Phi_1^\dagger\Phi_1) + m_{22}^2(\Phi_2^\dagger\Phi_2) - m_{12}^2(\Phi_1^\dagger\Phi_2 + \Phi_2^\dagger\Phi_1) + \frac{\lambda_1}{2}(\Phi_1^\dagger\Phi_1)^2 + \frac{\lambda_2}{2}(\Phi_2^\dagger\Phi_2)^2 + \lambda_3(\Phi_1^\dagger\Phi_1)(\Phi_2^\dagger\Phi_2) + \lambda_4(\Phi_1^\dagger\Phi_2)(\Phi_2^\dagger\Phi_1) + \frac{\lambda_5}{2}[(\Phi_1^\dagger\Phi_2)^2 + (\Phi_2^\dagger\Phi_1)^2]. \quad (1)$$

After electroweak symmetry breaking (EWSB) the two $SU(2)_L$ doublets Φ_1 and Φ_2 can be expanded around their two vacuum expectation values (vevs) v_1 and v_2 , respectively, as

$$\Phi_1 = \begin{pmatrix} \phi_1^+ \\ \frac{1}{\sqrt{2}}(v_1 + \rho_1 + i\eta_1) \end{pmatrix}, \quad \Phi_2 = \begin{pmatrix} \phi_2^+ \\ \frac{1}{\sqrt{2}}(v_2 + \rho_2 + i\eta_2) \end{pmatrix}, \quad (2)$$

with the vev ratio given by $\tan \beta \equiv v_2/v_1$. The vevs satisfy the relation $v = \sqrt{v_1^2 + v_2^2}$ where $v \simeq 246$ GeV is the SM vev. The eight (scalar) degrees of freedom, $\phi_{1,2}^\pm$, $\rho_{1,2}$ and $\eta_{1,2}$, give rise to three Goldstone bosons, G^0 and G^\pm , and five physical scalar fields, two \mathcal{CP} -even scalar fields, h and H , where by convention $m_h < m_H$, one \mathcal{CP} -odd field, A , and one charged Higgs pair, H^\pm . The mixing angles α and β diagonalize the \mathcal{CP} -even and \mathcal{CP} -odd/charged Higgs mass matrices, respectively.

The occurrence of tree-level flavor-changing neutral currents (FCNC) is avoided by imposing a \mathbb{Z}_2 symmetry, only softly broken by the m_{12}^2 term in the Lagrangian. The extension of the \mathbb{Z}_2 symmetry to the Yukawa sector prohibits tree-level FCNCs. This results in four variants of the 2HDM, depending on the \mathbb{Z}_2 parities of the fermion types. In this article we focus on the Yukawa type I, where all the fermions couple only to Φ_2 .

Here we work in the physical basis of the 2HDM, where most of the free parameters in Eq. (1) are expressed in terms of a set of “physical” parameters given by

$$c_{\beta-\alpha}, \quad \tan \beta, \quad v, \quad m_h, \quad m_H, \quad m_A, \quad m_{H^\pm}, \quad m_{12}^2, \quad (3)$$

Table 1 Factors appearing in the couplings of the neutral Higgs bosons to fermions, $\xi_{h,H}^f$, and to gauge bosons, $\xi_{h,H}^V$, in the 2HDM of type I

	Type I
ξ_h^u	$s_{\beta-\alpha} + c_{\beta-\alpha} \cot \beta$
$\xi_h^{d,l}$	$s_{\beta-\alpha} + c_{\beta-\alpha} \cot \beta$
ξ_h^V	$s_{\beta-\alpha}$
ξ_H^u	$c_{\beta-\alpha} - s_{\beta-\alpha} \cot \beta$
$\xi_H^{d,l}$	$c_{\beta-\alpha} - s_{\beta-\alpha} \cot \beta$
ξ_H^V	$c_{\beta-\alpha}$

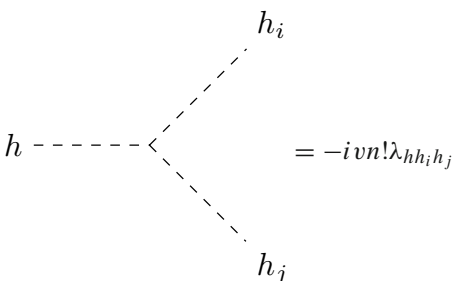
where we use the short-hand notation $s_x = \sin(x)$, $c_x = \cos(x)$. In our analysis we will identify the lightest \mathcal{CP} -even Higgs boson, h , with the one observed at the LHC at ~ 125 GeV.

The couplings of the Higgs bosons to SM particles are modified w.r.t. the SM Higgs-coupling predictions because of the mixing in the Higgs-boson sector. The couplings of the \mathcal{CP} -even neutral Higgs bosons to fermions and to gauge bosons are given by,

$$\mathcal{L} = - \sum_{f=u,d,l} \frac{m_f}{v} [\xi_h^f \bar{f} f h + \xi_H^f \bar{f} f H] + \sum_{h_i=h,H} \left[g m_W \xi_{h_i}^W W_\mu W^\mu h_i + \frac{1}{2} g m_Z \xi_{h_i}^Z Z_\mu Z^\mu h_i \right]. \quad (4)$$

Here m_f , m_W and m_Z are the fermion, W boson and Z boson masses, respectively. The modification factors in the couplings to fermions and gauge bosons, $\xi_{h,H}^f$ and $\xi_{h,H}^V$, for the 2HDM of type I are given in Table 1.

The generic triple Higgs coupling $\lambda_{hh_i h_j}$ involving at least one SM-like Higgs boson h is defined such that the Feynman rules are given by



$$h \text{ --- } \text{---} \begin{array}{l} \text{---} h_i \\ \text{---} h_j \end{array} = -i v n! \lambda_{hh_i h_j} \quad (5)$$

where n is the number of identical particles in the vertex. Relevant for our analysis here are λ_{hhh} and λ_{hhH} . We adopt this convention in Eq. (5) so that the light Higgs triple coupling λ_{hhh} has the same normalisation as λ_{SM} in the SM, which is given by $-6i v \lambda_{\text{SM}}$ with $\lambda_{\text{SM}} = m_h^2/2v^2 \simeq 0.13$. We furthermore define $\kappa_\lambda \equiv \lambda_{hhh}/\lambda_{\text{SM}}$.

The explicit expressions of the two triple Higgs couplings are given by

$$\begin{aligned}\lambda_{hhh} &= -\frac{1}{2} \left\{ \lambda_1 c_\beta s_\alpha^3 - \lambda_2 c_\alpha^3 s_\beta + (\lambda_3 + \lambda_4 + \lambda_5) \right. \\ &\quad \times \left. \left(c_\alpha^2 c_\beta s_\alpha - c_\alpha s_\alpha^2 s_\beta \right) \right\} \\ &= \frac{1}{2v^2} \left\{ m_h^2 s_{\beta-\alpha}^3 + \left(3m_h^2 - 2\bar{m}^2 \right) c_{\beta-\alpha}^2 s_{\beta-\alpha} \right. \\ &\quad \times \left. + 2 \cot 2\beta \left(m_h^2 - \bar{m}^2 \right) c_{\beta-\alpha}^3 \right\},\end{aligned}\quad (6)$$

$$\begin{aligned}\lambda_{hhH} &= \frac{1}{2} \left\{ 3\lambda_1 c_\alpha c_\beta s_\alpha^2 + 3\lambda_2 c_\alpha^2 s_\alpha s_\beta \right. \\ &\quad \left. + (\lambda_3 + \lambda_4 + \lambda_5) \left(c_\alpha^3 c_\beta - 2c_\alpha^2 s_\alpha s_\beta - 2c_\alpha c_\beta s_\alpha^2 + s_\alpha^3 s_\beta \right) \right\} \\ &= -\frac{c_{\beta-\alpha}}{2v^2} \left\{ \left(2m_h^2 + m_H^2 - 4\bar{m}^2 \right) s_{\beta-\alpha}^2 \right. \\ &\quad \left. + 2 \cot 2\beta \left(2m_h^2 + m_H^2 - 3\bar{m}^2 \right) s_{\beta-\alpha} c_{\beta-\alpha} \right. \\ &\quad \left. - \left(2m_h^2 + m_H^2 - 2\bar{m}^2 \right) c_{\beta-\alpha}^2 \right\},\end{aligned}\quad (7)$$

where \bar{m}^2 , derived from m_{12}^2 , is given by:

$$\bar{m}^2 = \frac{m_{12}^2}{\sin \beta \cos \beta}.\quad (8)$$

The triple Higgs couplings depend on $c_{\beta-\alpha}$. In particular, in the “alignment limit”, $c_{\beta-\alpha} \rightarrow 0$, where the light \mathcal{CP} -even Higgs couplings to the SM particles recover SM values, the triple Higgs couplings approach the values $\lambda_{hhh} = \lambda_{\text{SM}}$ and $\lambda_{hhH} = 0$, respectively.

2.2 Theoretical and experimental constraints

In this subsection we briefly summarize the various theoretical and experimental constraints considered in our analysis (more details can be found in Refs. [14, 15]). Note, that we did not check for constraints arising from di-Higgs measurements at the LHC. The analysis performed in [6] showed that non-resonant and resonant di-Higgs searches start to cut in the parameter spaces of extended Higgs sector models. However, the parameter spaces of the \mathcal{CP} -conserving 2HDM investigated here are not affected yet.

• Theoretical constraints

The important theoretical constraints come from tree-level perturbative unitarity and stability of the electroweak vacuum. They are ensured by an explicit test of the underlying Lagrangian parameters (details of our approach can be found in Ref. [14]). The parameter space allowed by these two constraints can be enlarged, if we

allow for a mass term breaking the imposed \mathbb{Z}_2 symmetry softly, i.e. we choose a non-zero m_{12}^2 . In some of the sample scenarios that we will investigate later, we chose m_{12}^2 as

$$m_{12}^2 = \frac{m_H^2 \cos^2 \alpha}{\tan \beta}.\quad (9)$$

This choice prevents λ_1 to receive large corrections for large $\tan \beta$ and ensures a larger allowed region by theoretical constraints when close to the alignment limit [31].

- **Constraints from electroweak precision data**
For SM extensions based solely on extensions of the Higgs sector the constraints from the electroweak precision observables (EWPO) can be expressed in terms of the oblique parameters S , T and U [32, 33]. Most constraining in the 2HDM is the T parameter, requiring either $m_{H^\pm} \approx m_A$ or $m_{H^\pm} \approx m_H$. In Ref. [14] three scenarios were defined to meet this constraint: (A) $m_{H^\pm} = m_A$, (B) $m_{H^\pm} = m_H$, and (C) $m_{H^\pm} = m_A = m_H$. Here it should be kept in mind that the EWPO used to set these constraints do not take into account the recent measurement of m_W at CDF [34], which deviates from the SM prediction by $\sim 7\sigma$. After this result for m_W was published, many articles appeared to describe the CDF value in BSM models, including analyses in the 2HDM, see Refs. [35–37] for the first papers. It was shown that the large m_W value can be accommodated by introducing a certain amount of splitting between the masses of the heavy 2HDM Higgs bosons. This also holds (albeit with a smaller amount of splitting) if a possible new world average, see Ref. [38], is taken into account [39]. However, we will not include this possibility into our analysis.
- **Constraints from direct Higgs-boson searches at colliders**
The exclusion limits at the 95% confidence level of all relevant BSM Higgs boson searches (including Run 2 data from the LHC) are included in the public code `HiggsBounds v. 5.9` [40–44].³ For a parameter point in a particular model, `HiggsBounds` determines on the basis of expected limits which is the most sensitive channel to test each BSM Higgs boson. Then, based on this most sensitive channel, `HiggsBounds` determines whether the point is allowed or not at the 95% CL. As input `HiggsBounds` requires some specific predictions from the model, like branching ratios or Higgs couplings, that were computed with the code `2HDMC-1.8.0` [46].⁴
- **Constraints from the properties of the ~ 125 GeV Higgs boson**

³ See Ref. [45] for the latest version.

⁴ Alternatively, the code `HDECAY` [47, 48] can be used. For a comparison of the two codes, see [49].

Any model beyond the SM has to accommodate a Higgs boson with mass and signal strengths as they were measured at the LHC. In the parameter points used the compatibility of the \mathcal{CP} -even scalar h with a mass of 125.09 GeV, h_{125} , with the measurements of signal strengths at the LHC is tested with the code `HiggsSignals v.2.6` [50–52]. The code provides a statistical χ^2 analysis of the h_{125} predictions of a certain model compared to the measurement of Higgs-boson signal rates and masses from the LHC. As for the BSM Higgs boson searches, the predictions of the 2HDM have been obtained with 2HDMC [46]. For a 2HDM parameter point to be allowed it was required [15] that the corresponding χ^2 is within 2σ ($\Delta\chi^2 = 6.18$) from the SM fit: $\chi^2_{\text{SM}} = 84.73$ with 107 observables.⁵

- Constraints from flavor physics

Constraints from flavor physics can be significant in the 2HDM, in particular because of the presence of the charged Higgs boson. Flavor observables like rare B decays, mixing parameters of B mesons, and LEP constraints on Z decay partial widths etc. are sensitive to charged Higgs boson contributions [53,54]. To test the parameter space, taking into account the most constraining decays $B \rightarrow X_s \gamma$ and $B_s \rightarrow \mu^+ \mu^-$, the code `SuperIso` [55,56] was used, again with the model input given by 2HDMC (see Ref. [14] for more details).

2.3 Benchmark planes

As a starting point for our study we take the analysis performed in Ref. [14], where the goal was to look for large deviations of BSM THCs in the 2HDM that are in agreement with present theoretical and experimental constraints. The analysis in this reference was done by performing a larger scan allowing the variations of all relevant free parameters in the 2HDM. The chosen benchmarks exhibit the largest deviations found in the THCs, which we expect can have an impact on the di-Higgs cross section, and therefore large deviations from the SM predictions can be found. Therefore, we define four benchmark planes that presumably exhibit an interesting phenomenology w.r.t. the di-Higgs production cross sections in the gluon fusion channel, $gg \rightarrow hh$. The planes furthermore exhibit certain specific aspects of the 2HDM phenomenology of di-Higgs production. The Yukawa type does not play an important role in the process $gg \rightarrow hh$, since the top Yukawa couplings, which are most relevant, are identical in the four types. On the other hand, it is desirable to be away from the alignment limits, to allow for a sizable λ_{hhH} , which can have an important impact via the resonant

H exchange in the s -channel (see also the discussion in the next section). Consequently, the the four planes are all chosen to be in the 2HDM Yukawa type I, as this type allows for larger deviations from the alignment limit taking into account the experimental constraints. The parameters are chosen as:

1. $m_{H^\pm} = m_H = m_A = 1000$ GeV, m_{12}^2 fixed via Eq. (9), free parameters: $c_{\beta-\alpha}$, $\tan \beta$
Expected features: small H contribution, variation of top Yukawa couplings and of λ_{hhh} and λ_{hhH} .
2. $m_{H^\pm} = m_H = m_A = 650$ GeV, $\tan \beta = 7.5$, free parameters: $c_{\beta-\alpha}$, m_{12}^2
Expected features: possibly relevant H contribution, variation of top Yukawa couplings and of λ_{hhh} and λ_{hhH} .
3. $\tan \beta = 10$, m_{12}^2 fixed via Eq. (9), free parameters: $c_{\beta-\alpha}$, $m_{H^\pm} = m_H = m_A$
Expected features: variation of the relevance of the H exchange contribution, variation of top Yukawa couplings and λ_{hhH} , including the alignment limit for $c_{\beta-\alpha} \rightarrow 0$.
4. $\tan \beta = 10$, $c_{\beta-\alpha} = 0.2$, m_{12}^2 fixed via Eq. (9) free parameters: m_H , $m_A = m_{H^\pm}$
Expected features: variation of the relevance of the H exchange contribution, variation of top Yukawa couplings and λ_{hhH} , always away from the alignment limit.

3 Cross section results

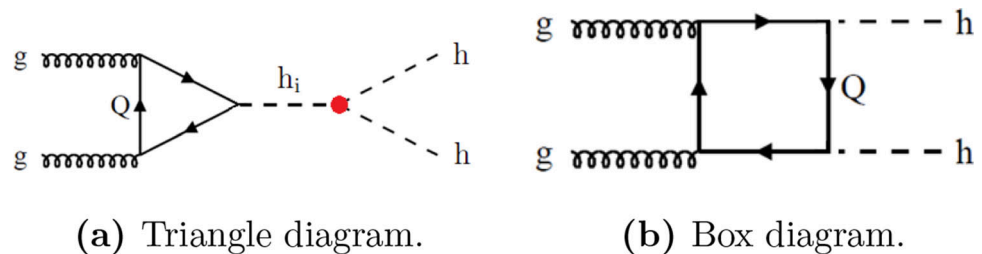
In this section we start our numerical analysis with the evaluation of the di-Higgs production cross sections in the benchmark planes defined in Sect. 2.3. We first discuss details of the calculation and then present the results, where we analyze the impact of a possible heavy Higgs, H , in the s -channel. We perform this analysis in all benchmark planes listed above to give a broad overview about the possible phenomenology of di-Higgs production in the 2HDM. In the following sections we will discuss selected planes and points to further examine the effects of the various triple Higgs couplings and the properties of the heavy \mathcal{CP} -even Higgs boson.

3.1 Calculation of $gg \rightarrow hh$

The main di-Higgs production process at the LHC is given by gluon fusion. The diagrams contributing at leading order are shown in Fig. 1. They both involve a heavy quark loop (top or bottom), where for small $\tan \beta$ the bottom-quark loop only plays a minor role. In the SM the triangle diagram, Fig. 1a, gives access to the trilinear Higgs coupling, λ_{hhh} , with the SM Higgs exchange in the s -channel. The box diagram, Fig. 1b, interferes destructively with the triangle diagram, resulting in a small cross section. In BSM theories additional diagrams can contribute. In particular in the case of the 2HDM the

⁵ These values have changed with the latest `HiggsSignals` version [45], but we do not expect a qualitative impact of this change on our results.

Fig. 1 Leading-order diagrams to SM-like Higgs pair production in gluon fusion processes at hadron colliders. The red dot shows the triple Higgs coupling, and $h_i = h, H$



second \mathcal{CP} -even Higgs can be exchanged in the s -channel, involving λ_{hhH} . This diagram will usually be referred to as the “resonant diagram”,⁶ whereas the SM-like contributions will be referred to as “the continuum”. Note that the Yukawa coupling and the trilinear Higgs self-coupling λ_{hhh} of the SM-like Higgs boson h can deviate from the SM values so that the observed destructive interference between the triangle and box diagram in the SM may not be effective.

For our numerical evaluation we use the code HPAIR [6, 29, 30, 57], adapted to the 2HDM. The original code evaluates the cross section of the production of two neutral Higgs bosons through gluon fusion at the LHC for the SM and the MSSM. The calculation is done at leading order (LO, see Fig. 1), and includes next-to-leading order (NLO) QCD corrections in the heavy top-mass limit. In this limit, it is assumed that the contribution of the bottom quark is negligible (it would introduce modifications of less than 1% in the SM) and then the top mass is taken to infinity. This assumption becomes less accurate at high values of $\tan \beta$ because the bottom quark loop contribution gets larger.

At LO the calculation includes top- and bottom-quark loops with full mass dependence. It is equivalent to the calculation done in the Minimal Supersymmetric Standard Model (MSSM) since its Higgs sector is equivalent to the 2HDM Type II. The only changes that are implemented in the case of the 2HDM are the modifications of the Yukawa couplings of the MSSM according to Table 1, for the corresponding type and the change of the triple Higgs couplings.⁷ As the QCD corrections in the heavy top-quark limit only involve couplings between coloured particles, they can straightforwardly be taken over from the MSSM to the 2HDM. For further details, we refer to Refs. [6, 29, 30, 57].

Whenever we present NLO results in the following, these are based on the evaluation with the modified HPAIR code, i.e. in the heavy top-mass, $m_t \rightarrow \infty$, limit (HTL). This is the most accurate prediction that can be used for the 2HDM case with the publicly available tools. For the SM the NLO QCD corrections have been provided including the full top quark

mass dependence [58–62]. The next-to-next-to-leading order (NNLO) corrections have been obtained in the large m_t limit [63, 64], the results at next-to-next-to-leading logarithmic accuracy (NNLL) became available in [65, 66], and the corrections up to next-to-next-to-leading order (N^3 LO) were presented in [67–70] for the heavy top-mass limit.⁸ From the NLO results including the full top-mass dependence [58–62] it is known, that the top-mass effects reduce the Born-improved HTL result (i.e. the cross section including the full top-mass dependence at LO and the NLO result in the HTL) by about 15%. This is worse for distributions, where it was found that the top mass effects result in a total modification of the differential cross section of up to -30% compared to the Born-improved HTL at large invariant mass values, for a c.m. energy of 14 TeV. An assessment of the theory uncertainties originating from the scheme and scale choice of the virtual top mass was provided in [62] and found to be significant. Combined with the factorization scale uncertainties they range between $+6\%$ and -23% for the total cross section at 14 TeV center of mass energy.

Recently, for the 2HDM the full NLO QCD corrections have been provided for the production of a mixed Higgs pair Hh and for a pair of pseudoscalars, AA , respectively, [73], with similar findings for the distributions, which increase with large invariant mass reaching -30% (-20%) in hH (AA) production at an invariant mass of 1.5 TeV. The mass effects hence not only change the absolute value of the cross section but also the shape of the distribution, so that the heavy top-mass approximation does not work as good as for the inclusive cross section (see also [74]). So far, however, there is no public code available that allows to compute the top-quark mass effects on the distributions for 2HDM Higgs pair production, in particular not for the interesting case of intermediate resonant heavy Higgs production, which we investigate here. In view of a missing code, we take the best prediction available at the moment and resort to the NLO QCD corrections in the heavy-top limit with the here mentioned caveats.⁹ Since we will investigate several distinct bench-

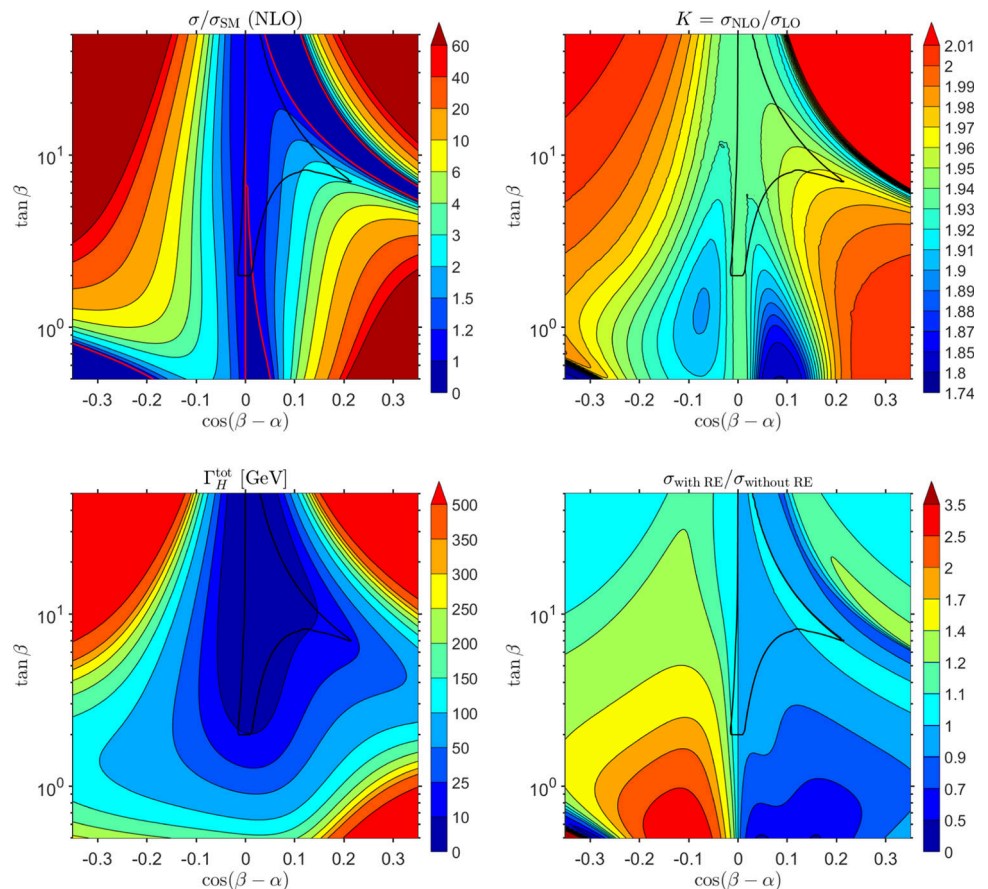
⁶ Owing to the fact that for $m_H > 2m_h$ the H can be resonantly produced which can largely enhance the di-Higgs cross section w.r.t. to the SM value. However, also scenarios with $m_H < 2m_h$ can be realized in the 2HDM where no such enhancement is observed. Still, for simplicity of the notation, we will call it “resonant diagram”.

⁷ It should be noted that HPAIR for the MSSM does not include any squark loop contributions.

⁸ For a review of higher-order corrections to SM di-Higgs production, see [8]. Recently, also first electroweak corrections have been provided in [71, 72].

⁹ Our benchmarks also contain heavy Higgs bosons with masses above the top mass value which questions the applicability of the heavy-top limit in the QCD corrections. The finite top-mass effects can be roughly

Fig. 2 Plane 1. 2HDM type I, $\tan \beta$ versus $c_{\beta-\alpha}$. Upper left: Cross section prediction for di-Higgs production in 2HDM normalized to the SM value, both evaluated at NLO QCD in the heavy top-quark limit. Allowed area inside the black contour. Red lines indicate the values at which the ratio is 1 (i.e. $\sigma = \sigma_{\text{SM}}$). The color coding indicates the size of this ratio. Upper right: K -factor, defined as the ratio of the NLO and LO cross sections. Lower left: Total decay width of the heavy Higgs H . Lower right: Ratio of the cross section with and without resonant enhancement, both evaluated at LO



mark cases and analyze what issues in general can arise in the measurement of trilinear Higgs self-couplings, this will still give us new insights despite the used approximations. The overall conclusions will remain the same: They will represent the best case scenario, assuming the distributions are changed uniformly at NLO. In this way, they show what at least can be expected.

3.2 Analysis of the cross section predictions

In Figs. 2, 3, 4 and 5 we show the results for the di-Higgs production cross section in the 2HDM normalized to the SM value calculated at NLO QCD in the Born-improved HTL for the gluon fusion process. The SM prediction was obtained with HPAIR assuming the alignment limit and coincides with the values given in Ref. [6],¹⁰

$$\begin{aligned}\sigma_{\text{SM}}^{\text{LO}}(pp \rightarrow hh) &= 19.76 \text{ fb}, \\ \sigma_{\text{SM}}^{\text{NLO}}(pp \rightarrow hh) &= 38.24 \text{ fb},\end{aligned}\quad (10)$$

estimated from the NLO QCD results in the SM including the full top-quark dependence. They amount to about 20% for heavy Higgs masses around 500 GeV, increasing to about 30% for Higgs mass values of 1 TeV.

¹⁰ As the NLO corrections are computed in the heavy top-quark limit it differs from the NLO SM-value including the full mass dependence [58–62].

The results for all the benchmark planes are shown as follows. In the upper left plot of each figure, we present the NLO 2HDM cross sections normalized to the NLO SM value, as indicated by the color coding. The red line shows where the ratio is one, and the inner part of the solid black line is allowed by all theoretical and experimental constraints (as evaluated in Refs. [14, 15]), see Sect. 2.2. The results away from the allowed region are also shown in order to see the general trends of the observables, but large deviations away from the allowed region signal deviations from the perturbative regime and should not be further analyzed. The upper right plot shows the K -factor, $K = \sigma_{\text{NLO}}/\sigma_{\text{LO}}$ of the 2HDM hh cross sections. It should be noted that for the determination of the K -factor we consistently evaluated the LO cross section with LO PDFs and the strong coupling α_s at LO, and the NLO cross section with NLO PDFs and α_s at NLO, we used CT14lo (for LO) and CT14nlo (for NLO) PDF sets [75–77]. The lower left plot indicates the total width of the heavy \mathcal{CP} -even Higgs boson, which contributes via the s -channel diagram (Fig. 1a with $h_i = H$). This quantity will be relevant for the discussion of the dependence of the cross section on the underlying parameter space. In some parts of the shown parameter space the ratio Γ_H/m_H reaches values $\gtrsim 0.5$. However, this happens far outside the allowed region, as indicated by the black solid line and thus does

Fig. 3 Plane 2. 2HDM, type I, m_{12}^2 versus $c_{\beta-\alpha}$. Otherwise plots as in Fig. 2

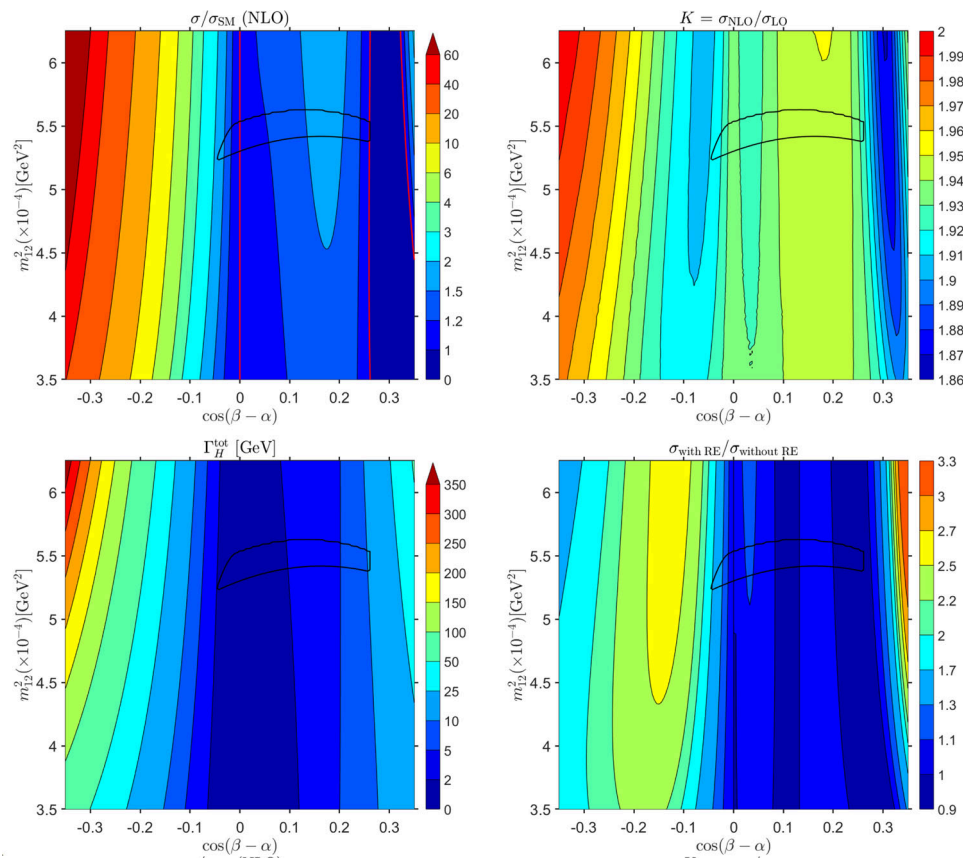


Fig. 4 Plane 3. 2HDM type I, $m_H = m_A = m_{H^\pm}$ versus $c_{\beta-\alpha}$. Otherwise plots as in Fig. 2

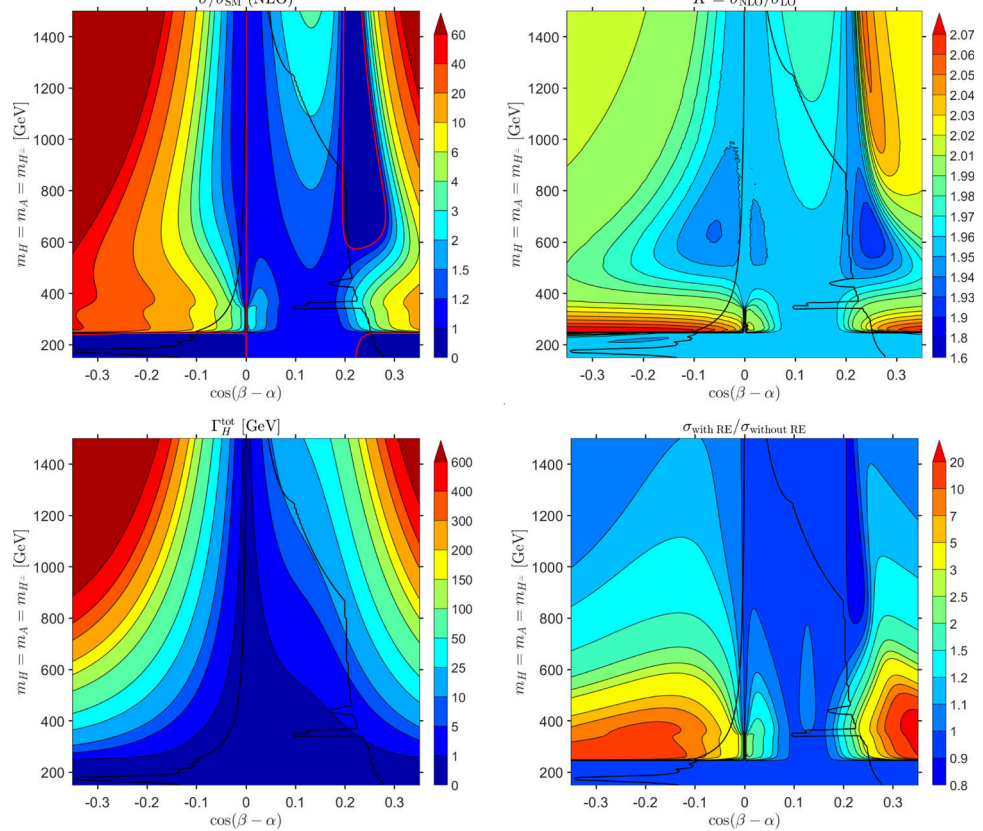
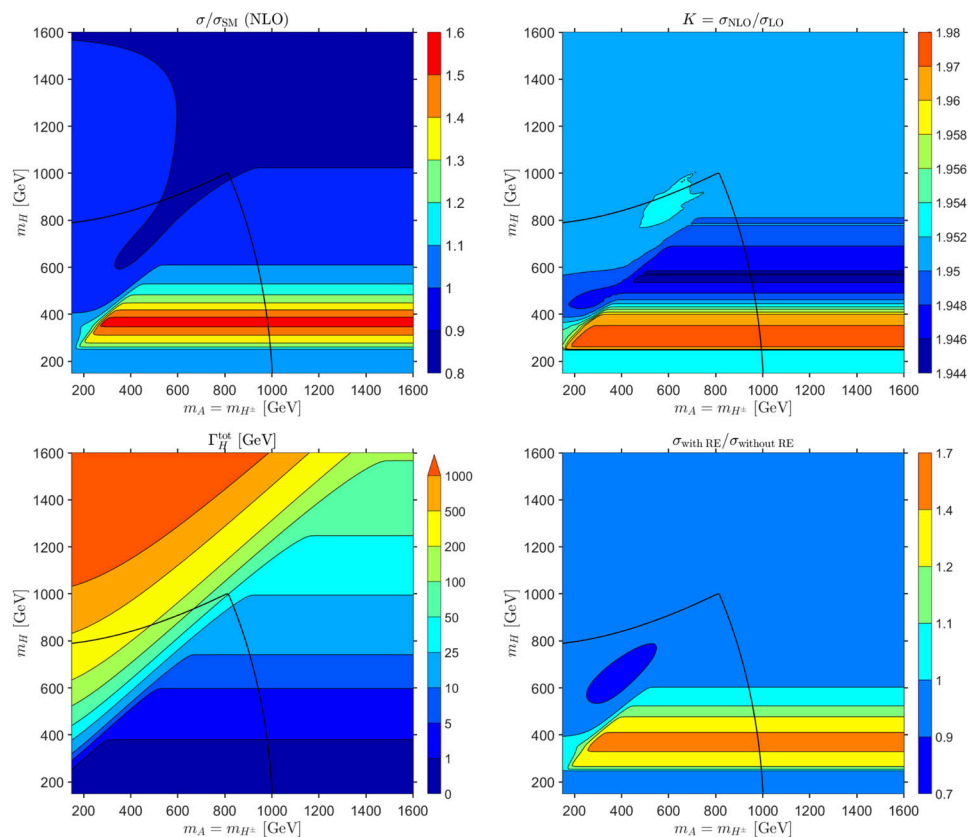


Fig. 5 Plane 4. 2HDM type I, m_H versus $m_A = m_{H^\pm}$. Otherwise plots as in Fig. 2



not have phenomenological consequences. Finally, the lower right plot shows the ratio of the full cross section, divided by the cross section obtained omitting the diagram with H in the s -channel, both evaluated at leading order. Large deviations from unity indicate an important contribution from the resonant H diagram.

The analysis for the benchmark plane 1 is presented in Fig. 2, where $\tan \beta$ is plotted against $c_{\beta-\alpha}$ for the four quantities described in the previous paragraph. In this scenario the heavy \mathcal{CP} -even Higgs mass is set to $m_H = 1000$ GeV.¹¹ We observe that the maximum deviation from the SM prediction within the allowed area occurs precisely at the “tip” that is furthest away from the alignment limit $c_{\beta-\alpha} = 0$ (see upper left plot). Here the enhancement factor in the cross section is ~ 3 . This corresponds to the minimum size of the triple Higgs coupling λ_{hhh} that was obtained in the allowed region of this benchmark plane ($\kappa_\lambda \sim -0.4$). If a deviation between the SM prediction and experiment is observed, this could point to a deviation of the κ_λ coupling. The dark blue region in this plot indicates that the production cross section is smaller than the SM prediction, as the ratio drops to $\sigma/\sigma_{SM} \lesssim 1$. The decrease here is of order 1% due to minor changes in the top Yukawa coupling in the 2HDM. The K -

factor in this benchmark plane results in a factor close to 2, more specifically in the allowed region of ~ 1.92 to ~ 1.97 (upper right plot). One can see that the decay width of H in this region can amount to ~ 25 GeV (lower left plot). A large total width Γ_H^{tot} has a suppressing effect on the H contribution to the cross section due to its appearance in the denominator of the s -channel propagator, as will be discussed below. We see that the H contribution has no enhancing effect on hh production within the allowed area given by the black lines (lower right plot). Including the resonance either slightly suppresses the cross section or leaves it unchanged (we find the ratio 1 exactly at the “tip”, where the hh cross section is maximal within the allowed region). In conclusion, in this plane the maximum enhancement of the cross section is precisely due to the deviation of the triple Higgs coupling from the expected SM value.

In the case of the benchmark plane 2, shown in Fig. 3, where we now plot m_{12}^2 versus $c_{\beta-\alpha}$, it can be observed that the cross section does not have a significant enhancement in the allowed region, as it does not even reach a factor of ~ 2 times the SM value. Also for this benchmark plane we observe that the largest value of the cross section falls in the region of the minimum value of κ_λ , i.e. where the destructive interference between box diagram and h exchange is minimal. The K factor in the allowed region is roughly ~ 1.91 to ~ 1.95 , again close to 2. In the evaluation of the effect of the heavy Higgs H , we observe that neither the decay widths

¹¹ For such high values one might consider an EFT analysis, rather than an analysis in a UV-complete model. However, since the aim of this section is the comparison of the case of larger and smaller m_H values, we refrain from such an analysis.

nor the resonant enhancement are significant in the allowed region. The H contribution almost has no effect on the hh production cross section.

In the benchmark plane 3, shown in Fig. 4, where we plot $m_H = m_A = m_{H^\pm}$ against $c_{\beta-\alpha}$, we allow for a variation of the heavier Higgs masses by fixing the value of $\tan\beta$ and the mass m_{12}^2 according to the Eq. (9). Concerning the normalized NLO cross section there is no enhancement below 250 GeV since the heavy Higgs is not produced on-shell. Above this threshold there is resonant enhancement due to the contribution of the heavy Higgs in the s -channel. In particular, the cross section is enhanced by up to a factor of ~ 8 in the “tail” at $c_{\beta-\alpha} \sim -0.1$. In this region one finds κ_λ close to 1, so that the enhancement of the cross section w.r.t. the SM is given by the diagram with H in the s -channel that resonantly decays into hh . This can also be seen in the lower right plot of Fig. 4, where a ratio of resonant over non-resonant cross section of up to ~ 8 is found. In this case there are two distinct regions of a suppression of the production cross section w.r.t. the SM. In particular, for values of $m_H < 250$ GeV, the decay $H \rightarrow hh$ is kinematically disallowed and the production cross section is small. The second region is found for values of $c_{\beta-\alpha} \sim 0.2$ and large m_H and is due to an enhanced prediction for κ_λ . When resonant production is suppressed, as starts to happen for higher values of m_H , the cross section is more sensitive to deviations in κ_λ . The dependence of the cross section on the value of κ_λ is quadratic and reaches a minimum for $\kappa_\lambda \sim 2.5$ located within the dark blue region. This trend is well known in literature and is the underlying explanation of the suppression in this parameter region. The K -factor in the maximally enhanced region is slightly above 2 (up to ~ 2.06).

Since in this plane we allow for a variation of the mass of the heavy Higgs in the propagator one can observe the enhancement of the cross section around $m_H \sim 350 - 400$ GeV that is expected from single Higgs production above the di-top threshold, $m_H \sim 2m_t$. This feature will be noted several times further in the text whenever m_H is a free parameter as well as for m_{hh} distributions. In this benchmark plane the enhancement due to the di-top production threshold is clearly visible in the lower right plot of Fig. 4 (particularly for negative $c_{\beta-\alpha}$ within the allowed region).

The final plane we investigate in detail is plane 4 as shown in Fig. 5. Here the two free parameters, that we plot against each other, are m_H and $m_A = m_{H^\pm}$. Correspondingly, one expects a large enhancement of the 2HDM cross section for $m_H \sim 400$ GeV where $m_H > 2m_h$ and above the di-top threshold. Exactly this can be observed in the upper left plot (total cross section) and the lower right plot (relative enhancement from the resonant diagram). The cross section can be up to 60% larger than the SM di-Higgs production cross section, with a K factor again close to 2. The total width of the heavy \mathcal{CP} -even Higgs ranges from very small values up to

larger than 200 GeV within the allowed region (found for low $m_A = m_{H^\pm}$ and large m_H). For large total widths the resonance enhancement is not effective. The largest enhancements of the cross section are found for relatively small values of $\Gamma_H^{\text{tot}} \lesssim 10$ GeV.

3.3 Dependence on triple Higgs couplings

In this subsection we analyze the cross section with respect to the triple Higgs couplings involved in the di-Higgs production process. In particular, we will show in which part of the parameter space the total di-Higgs production cross section has a relevant dependence on λ_{hhh} and/or λ_{hhH} .

Here we focus on a statistical treatment of the errors of the total cross section measurement, which is assumed to be Gaussian, neglecting systematic uncertainties. It was found in Refs. [8, 78] that the statistical uncertainty of the total di-Higgs cross section measurement, assuming SM values, will reach a level of 4.5σ at the end of the HL-LHC, combining ATLAS and CMS. (Taking into account systematic effects could lower this value to $\sim 4\sigma$.) Consequently, we will approximate the corresponding error in the measurement as $\delta\mathbf{x}_S = \mathbf{x}_S/4.5$.¹² The significance of the deviation of the (to be measured) 2HDM cross section w.r.t. the SM value can then be expressed as

$$\Delta\sigma_{\text{SM}} \equiv \frac{\mathbf{x}_{\text{S2HDM}} - \mathbf{x}_{\text{SM}}}{\delta\mathbf{x}_S}. \quad (11)$$

It should be noted that this approximation becomes worse for larger deviations of $\mathbf{x}_{\text{S2HDM}}$ from \mathbf{x}_{SM} , since the precision of the measurements, $\delta\mathbf{x}_S$, has been evaluated assuming the SM value. For higher cross sections a more precise measurement can be expected. A more precise analysis is not possible because of the lack of corresponding experimental analyses.

We present our results within the four benchmark planes discussed above in Figs. 6, 7, 8, 9 and 10. For each plane in the upper left and middle plot we will show the predictions of κ_λ and λ_{hhH} , as obtained in Refs. [14, 15]. The upper right plot, for better comparison, repeats the results of $\sigma_{\text{2HDM}}/\sigma_{\text{SM}}$ at NLO QCD as presented in the upper left plots in Figs. 2, 3, 4 and 5, where we here also show the maximum (minimum) value of the coupling that is realized within the allowed region as red (blue) dots. The three upper plots are always given in the plane of the two free parameters involved in the respective benchmark choice. The lower left plot shows which combinations of κ_λ and λ_{hhH} can be reached in each plane, where the points inside the area allowed by theoretical and experimental constraints are marked in red (and indicated with a red

¹² It should be noted that we usually denote the cross section as σ , but in this discussion we change our notation to \mathbf{x}_S since it can be misunderstood as the standard deviation in statistics which is also denoted as σ .

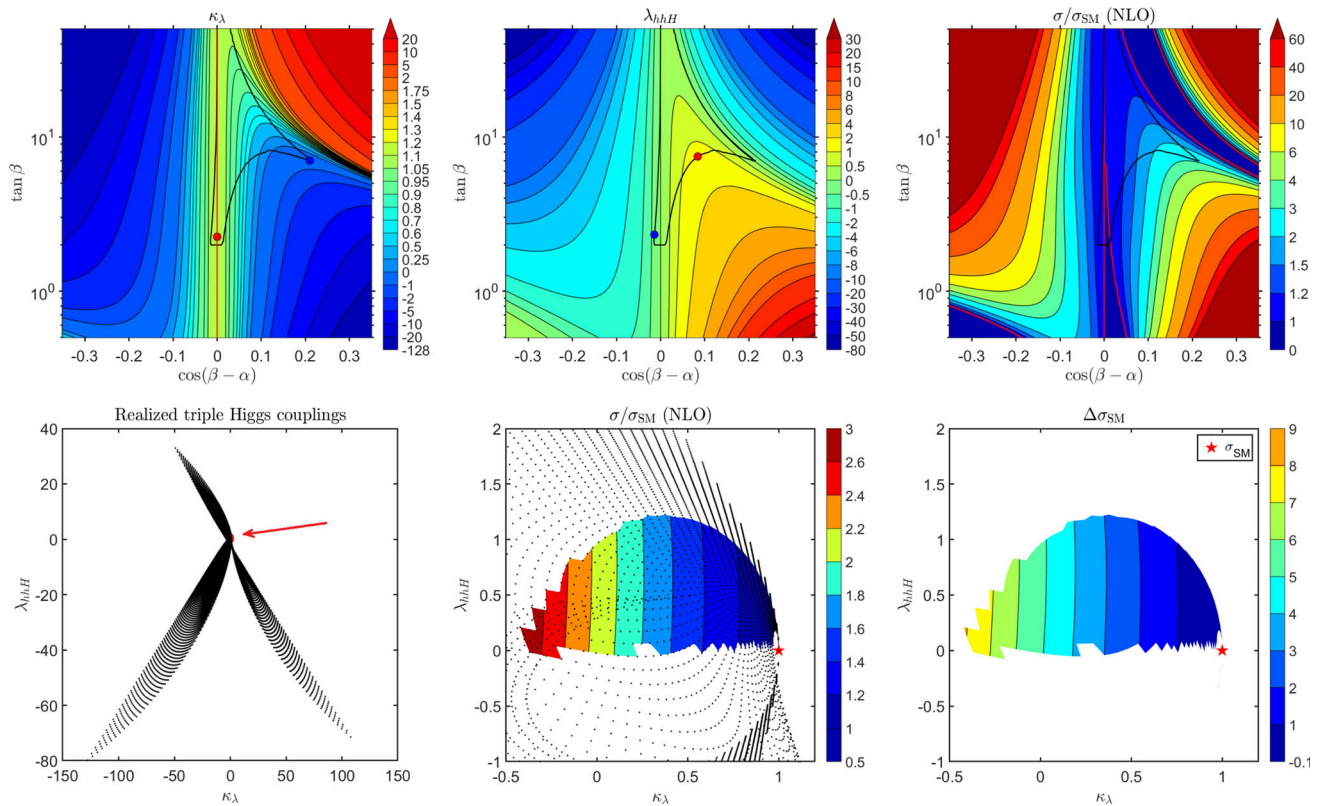


Fig. 6 Plane 1. Upper line: triple Higgs coupling predictions in the 2HDM and value of the normalized cross section (w.r.t. the SM value) evaluated at NLO QCD in the same parameter space. Red (blue) dots show the maximum (minimum) value of the trilinears that is realized in the allowed region. Lower left: points realized in the couplings plane, the red area around $\kappa_\lambda = 1$ and $\lambda_{hhH} = 0$ represents the points that fall into the allowed region, indicated by a red arrow. Lower middle: zoom

into the previous plot, color code indicates the normalized cross section within the allowed region for different values of triple Higgs couplings. Black dots indicate the existent scan parameter points in the κ_λ - λ_{hhH} plane within and outside the allowed region that was obtained from the figures in the upper row. The red star indicates the SM limit ($\kappa_\lambda = 1$ and $\lambda_{hhH} = 0$). Lower right: expected sensitivity to the deviation of the cross section from the SM value. Red star indicates the SM

arrow). The lower middle plot, focusing on the allowed region in the κ_λ - λ_{hhH} plane, presents the values of $\sigma_{2\text{HDM}}/\sigma_{\text{SM}}$ at NLO QCD in this plane (with the SM point $\kappa_\lambda = 1$, $\lambda_{hhH} = 0$ marked by a red star). This indicates the dependence of the total 2HDM di-Higgs production cross section on the two involved triple Higgs couplings. The black points represent the values of the THCs that are reached in this plane. The lower right plot shows the same area in the κ_λ - λ_{hhH} plane, now indicating the expected number of $\Delta\sigma_{\text{SM}}$, see Eq. (11), that the (to be measured) 2HDM result differs from the SM prediction, i.e. with which significance such a deviation can be measured experimentally.

In benchmark plane 1, Fig. 6, one can observe from the comparison of the upper left and right plots that within the allowed range, as discussed above, the smallest κ_λ value gives rise to the largest value of $\sigma_{2\text{HDM}}$. As can be inferred from the lower middle plot, in this benchmark plane the cross section depends strongly on κ_λ , but effectively not on λ_{hhH} . This is due to the fact, as discussed above, that the heavy \mathcal{CP} -even Higgs is too heavy to give a sizable s -channel contribution.

Overall, one can observe that for the smallest allowed κ_λ values, $\kappa_\lambda \sim -0.4$, a cross section enhancement of up to ~ 3 can be found.

Finally, we see from the lower right plot that for the smallest κ_λ , corresponding to the largest $\sigma_{2\text{HDM}}$, a deviation of up to $\Delta\sigma_{\text{SM}} \sim 9$ can be expected. This indicates that within this 2HDM benchmark plane a clear distinction between the 2HDM and the SM via the di-Higgs production cross section can be possible. Deviations of more than 2σ can be expected for $\kappa_\lambda \lesssim 0.6$.

In benchmark plane 2 a similar result as in plane 1 can be observed, as shown in Fig. 7. The largest cross sections are found for the smallest κ_λ values, and the predicted 2HDM di-Higgs cross section depends only mildly on λ_{hhH} . The latter can again be understood because of the relatively large value of $m_H = 650$ GeV in this benchmark plane. The maximum significance of the 2HDM deviation w.r.t. the SM value is less than for plane 1 with a value of at most 3.5σ , reached for $\kappa_\lambda \sim 0.9$ and $\lambda_{hhH} \sim -0.5$.

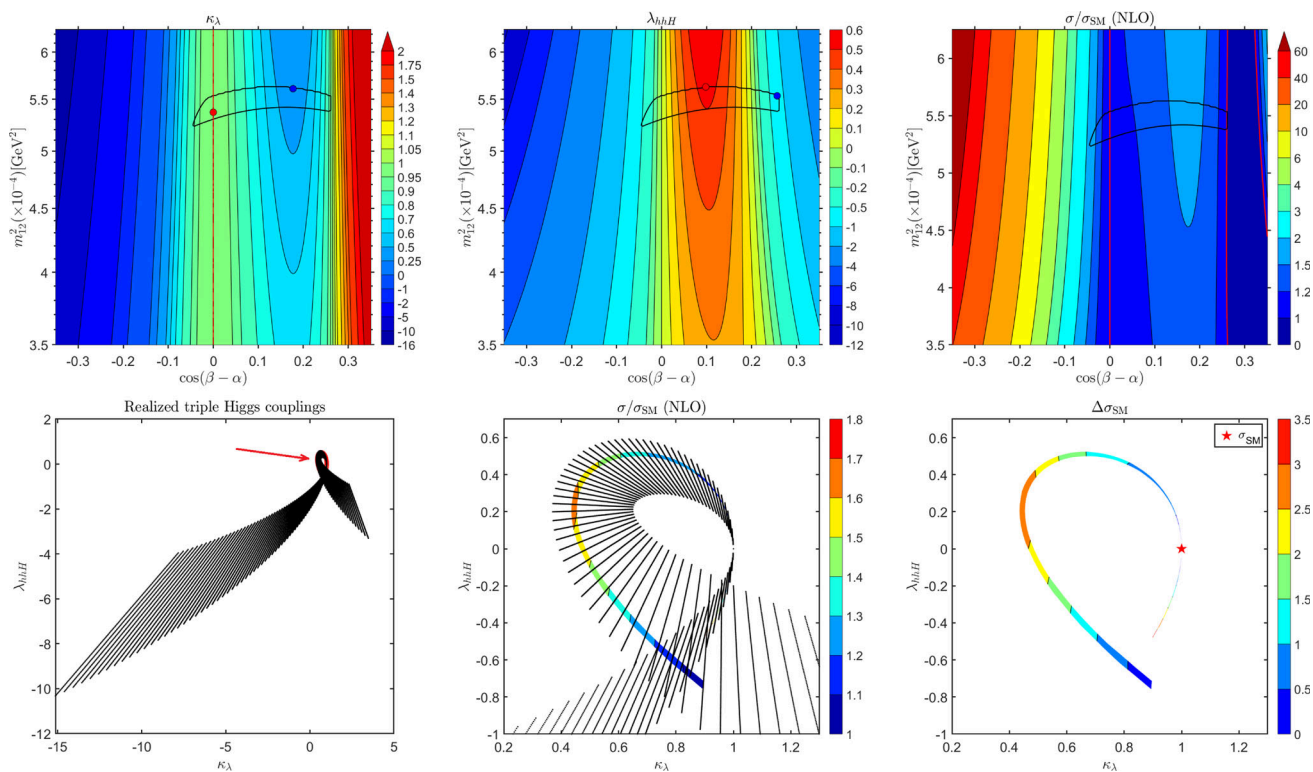


Fig. 7 Plane 2. 2HDM, type I, m_{12}^2 versus $c_{\beta-\alpha}$. Otherwise plots as in Fig. 6

The situation is more involved in plane 3, which we show in Fig. 8. As discussed in the previous subsection, very large enhancements can be reached in this parameter plane, and larger allowed regions are found for both signs of $c_{\beta-\alpha}$. The lower middle plot, showing the cross section enhancement w.r.t. the SM seems to show a relatively small enhancement of up to ~ 3 . The larger effects that actually occur (enhancements of up to ~ 8) are found in comparably small regions and are thus not well visible in this figure (but will be shown clearly below). The lower right plot shows the $\Delta\sigma_{SM}$, and for large parts of the parameter space we find the same feature as in the two benchmark planes above: the largest deviations are found for the smallest κ_λ values, and independent of λ_{hhH} , reaching about 5σ . However, some “overlaid” structure is visible around $\kappa_\lambda \sim 1$. Here the same combinations of κ_λ and λ_{hhH} are reached for different points in the parameter space, in particular for both signs of $c_{\beta-\alpha}$. To analyze this scenario in more detail we split up the plots for positive and negative $c_{\beta-\alpha}$.

In Fig. 9 we present the results where we have divided the allowed region of benchmark plane 3 and the obtained cross sections and their sensitivity in the couplings plane in positive and negative values of $c_{\beta-\alpha}$. The left (right) column in Fig. 9 shows the results for $c_{\beta-\alpha}$ negative (positive). The upper row indicates the combination of κ_λ and λ_{hhH} that can be reached in the full benchmark plane. The middle row

shows $\sigma_{2HDM}/\sigma_{SM}$, whereas the lower row indicates the level of $\Delta\sigma_{SM}$ that can be reached, where we have zoomed further into the interesting region. The middle left plot demonstrates that for κ_λ close to 1 the cross section can be strongly enhanced with the enhancement strongly depending on the BSM THC λ_{hhH} . This behavior can be traced back to the H contribution in the s -channel for relatively small values of m_H , as discussed in the previous subsections. Looking into the (zoomed in) result for $\Delta\sigma_{SM}$ (lower left plot) one can observe that for the smallest values of $\lambda_{hhH} \sim -0.2$ a deviation from the SM by up to 35σ can be expected. More importantly, the size of the deviation may give an indication of the value of λ_{hhH} . Going to positive values of $c_{\beta-\alpha}$ as presented in the right column, one can observe that for large parts of the parameter space a dependence solely on κ_λ is found, as in the previous benchmark planes. However, again for $\kappa_\lambda \sim 1$ strong enhancements are found due to the presence of the heavy \mathcal{CP} -even Higgs in the resonance. This is better visible in the lower right plot (the “gap-like” structures originate from BSM Higgs-boson search limits, due to under-fluctuations for that mass in the experimental data), demonstrating that for small, but positive values of λ_{hhH} deviations of up to 6σ can be seen, whereas for negative values of $\lambda_{hhH} \sim -0.2$ even deviations of up to 9σ can be found. Finally, we also see that in some parameter regions, namely when $\sigma/\sigma_{SM} < 1$, the sensitivity to the THC wors-

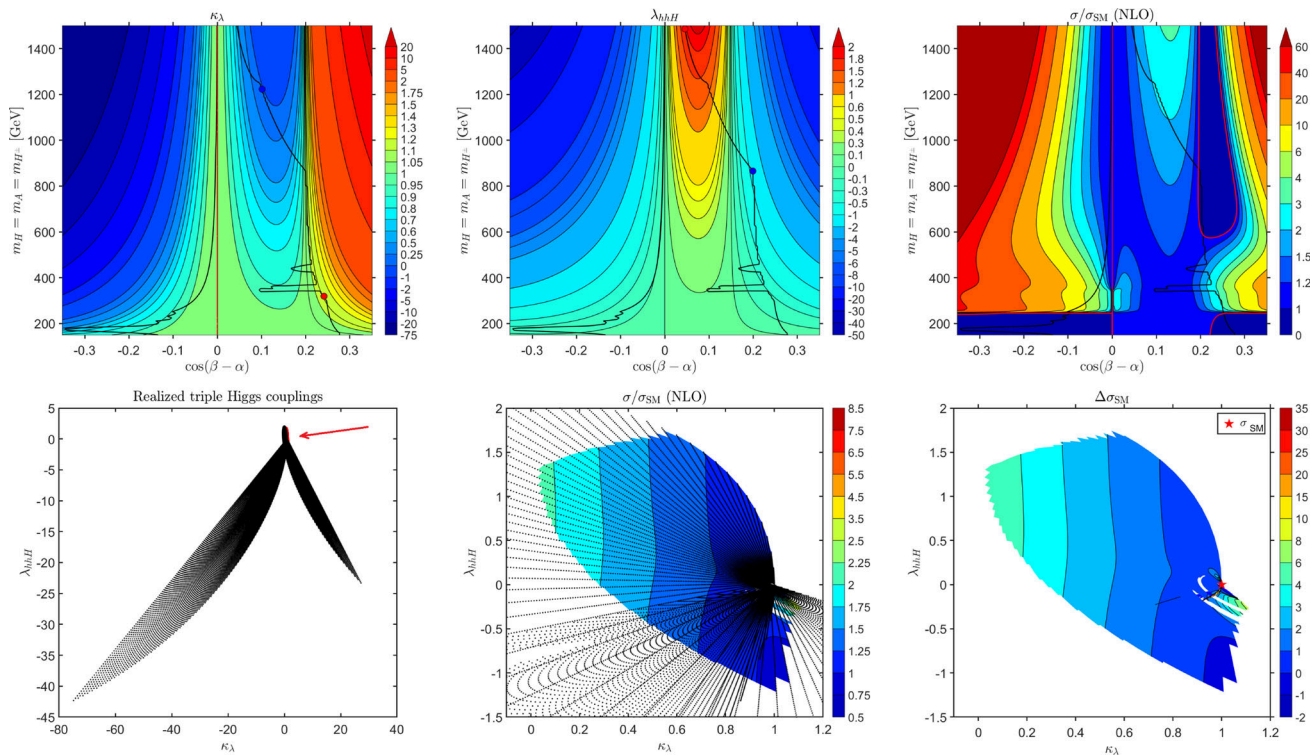


Fig. 8 Plane 3. 2HDM type I, $m_H = m_A = m_{H^\pm}$ versus $c_{\beta-\alpha}$. Otherwise plots as in Fig. 6

ens w.r.t the SM and the variable $\Delta\sigma_{\text{SM}}$ drops below 1. This means that we would need more statistics to measure the cross section and infer the values of the THC than expected in the SM. Here it should be kept in mind that this analysis only demonstrates the possible dependencies and effects of the THC on the di-Higgs production cross section. As will be discussed below, an actual possibility for a determination of λ_{hhH} (or κ_λ) is not implied, as it depends on the precise knowledge of the other (free) parameters.

Our final analysis in this section is done for benchmark **plane 4**, as shown in Fig. 10. In this $m_A = m_{H^\pm} - m_H$ plane the value of κ_λ is always close to 1, varying only by about $\sim 10\%$, so that large variations of the di-Higgs production cross section can only be produced by resonant enhancement. The coupling λ_{hhH} varies between 0 to ~ -1.5 in the allowed region (and even down to ~ -4.5 for the largest m_H values). The cross section, as discussed already in the previous subsection shows an interesting enhancement of up to $\sim 60\%$, where the heavy Higgs is resonant and not too heavy, $m_H \sim 400$ GeV. We will use the behavior of $\sigma_{2\text{HDM}}$ in this benchmark plane for a more detailed analysis of the invariant m_{hh} distribution in the next section.

The projection into the κ_λ - λ_{hhH} plane shows only a line, which can be understood as follows. Looking at Eqs. (6) and (7) and discarding all the terms proportional to constants (the angles α and β) we find the following relations:

$$\begin{aligned}\kappa_\lambda &= c_1 + c_2 \bar{m}^2, \\ \lambda_{hhH} &= c_3 + c_4 \bar{m}^2,\end{aligned}\quad (12)$$

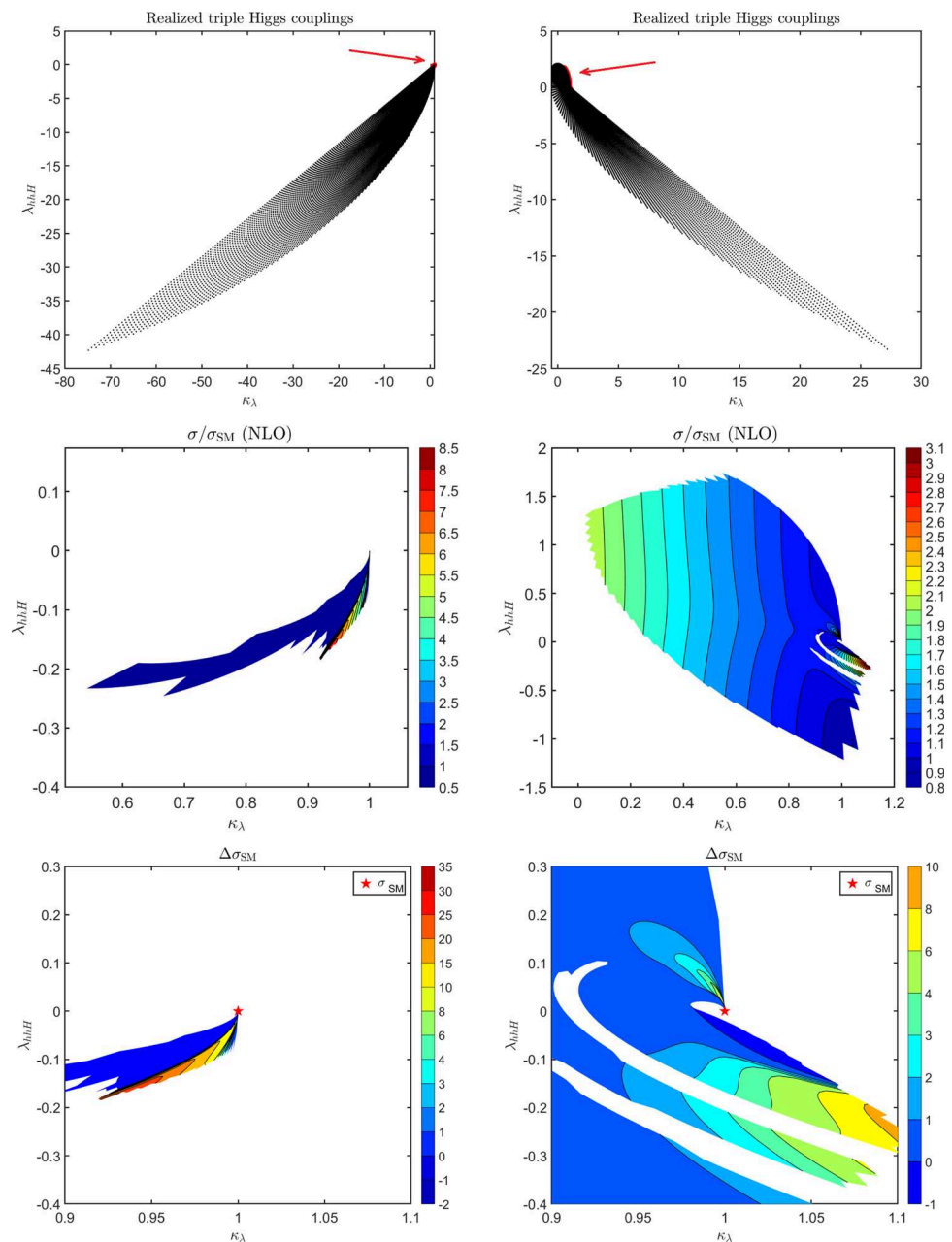
where the $c_{1,2,3,4}$ are constant terms, and it is taken into account that according to Eq. (9) $\bar{m}^2 \propto m_{12}^2 \propto m_H^2$. Consequently, one finds

$$\lambda_{hhH} = c_3 - \frac{c_1 c_4}{c_2} + \frac{c_4}{c_2} \kappa_\lambda, \quad (13)$$

resulting in the linear dependence that is observed in the lower plots of Fig. 10.

Now we proceed to analyze the values of the cross section that are possible for the different values of the THC, even though we do not have a truly 2-dimensional plot in these cases. For the benchmark plane 4, in the lower middle plot of Fig. 10 the cross section is badly defined in the sense that more than one value of the cross section corresponds to a particular value of the THC. This happens when we allow for a change in the masses but fix the angles, as discussed above. The THC change in a coherent way for different masses m_H (see upper left and middle plots in Fig. 10), while the cross section has different possible values. As an example, for m_H in the range ~ 220 GeV to ~ 800 GeV it can vary within $\sim (0.8 - 1.6) \times \sigma_{\text{SM}}$, as can be seen in the upper right plot. Therefore, in the lower middle plot we represented the mean value of the cross section as a circle for a particular combination of $(\kappa_\lambda, \lambda_{hhH})$. We show maximum (upper tri-

Fig. 9 Plane 3. Split for negative (left) and positive (right) values of $c_{\beta-\alpha}$. Upper line: allowed region. Middle line: total di-Higgs production cross section at NLO QCD w.r.t the SM. Lower line: expected sensitivity to the cross section deviation (zoomed into the interesting region)



angle “slightly displaced above the circles”) and minimum (lower triangle “slightly displaced below the circles”) values of the normalized cross section for this same combination of $(\kappa_\lambda, \lambda_{hhH})$. One can observe that the highest cross section is realized for a $\kappa_\lambda \sim 0.985$ and $\lambda_{hhH} \sim -0.2$. In this point the value of the cross section varies roughly from 1 to 1.6 and the sensitivity that can be reached in the most optimistic scenario (i.e. the largest deviation from the SM that is realized) is almost 2.5σ , as can be seen in the lower right plot. This enhancement is relatively small, but it demonstrates that in this plane the relevant role of the coupling λ_{hhH} is more significant than κ_λ , which is very close to 1, where these effects are found. The size of the deviation clearly depends on λ_{hhH} in this case.

Let us add a final word on the theory uncertainties. We outlined above that we have to rely on the NLO QCD corrections in the heavy-top limit. The higher-order corrections can, however, also change the shape of the distributions. Without an available calculation taking into account the NLO top-mass effects on the distributions, which is missing for the 2HDM case with resonant Higgs production, it is difficult and highly speculative to try to do an estimate, as can be seen from the at present available discussions on the theory uncertainties [62]. While a missing theory uncertainty estimate limits the interpretation of our results, they are still useful in the following sense. By investigating several benchmark points we get an overall picture that may also represent to some extent the impact of a changed shape. The latter

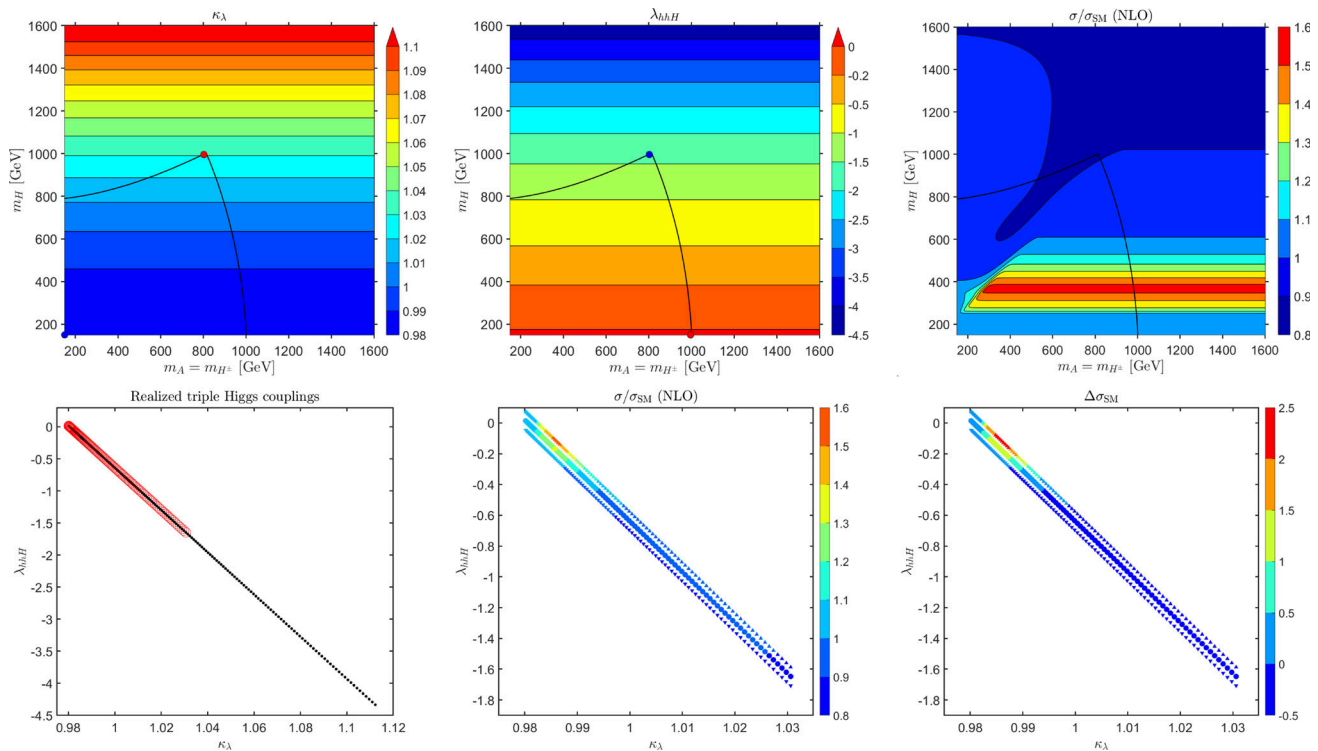


Fig. 10 Plane 4. 2HDM type I, m_H versus $m_A = m_{H^\pm}$. Otherwise plots as in Fig. 6

would lead to a modified relation between the observation and the input parameters. Furthermore, our results represent the best case by assuming a constant K -factor for the distributions and hence give us insights on what can in the best case be expected.

3.4 Conclusion from the cross section analysis

The four benchmark planes have been chosen to map out the different phenomenology that can be expected from the 2HDM in di-Higgs production, $gg \rightarrow hh$. This refers to the variation of the relevance of the H exchange contribution, as well as to the variation of the involved Yukawa couplings and in particular of the two relevant THCs, λ_{hhh} and λ_{hhH} .

It was demonstrated that the 2HDM cross section for $gg \rightarrow hh$ can differ substantially from the corresponding SM result. In most of the cases the deviation was found at the level of up to 3σ , but also 10σ or more can be found in extreme cases. Smaller variations arise from the deviations from $\kappa_\lambda = 1$. The largest deviations, however, were shown to arise from the H exchange contribution. For this analysis particularly the mapping of our parameter space onto the κ_λ – λ_{hhH} plane proved to be useful. The results are corroborated by the comparison of the calculation of the cross section including all diagrams in comparison with the calculation leaving out the H resonance contribution.

Furthermore, it could be observed (in agreement with Ref. [14]) that in the most extreme cases values of $\kappa_\lambda = [-0.5, 1.1]$ are found, where the lower range of these values would lead to an observable deviation at the HL-LHC.¹³

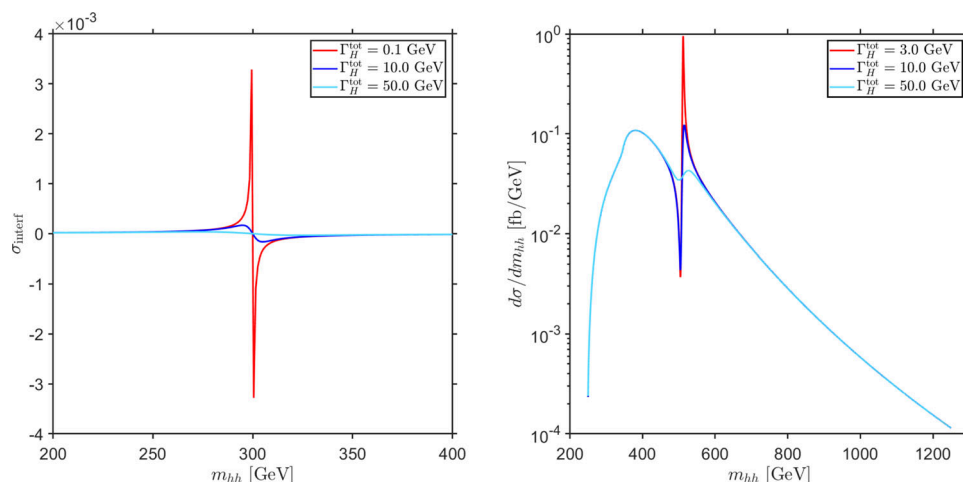
4 Analysis of m_{hh}

In the next step of our analysis we will study the influence of the THCs on the di-Higgs production cross sections by evaluating the di-Higgs invariant mass distribution, m_{hh} . We first demonstrate in a toy example the effect of the characteristic properties of the resonant Higgs boson: its mass, its width, and the sign of the coupling combination ($\lambda_{hhH} \times \xi_H^I$). Subsequently, the analysis will be performed for several benchmark points located in the planes discussed in the previous section, where the effects of the characteristics of the resonance will be demonstrated in a real model.

The invariant mass distributions, $d\sigma/dm_{hh}$, are also obtained with the code HPAIR. We will use a grid of values for the invariant mass m_{hh} that range from 250 GeV to 1250 GeV. As a default value we will use a bin size of 20 GeV (where experimentally a bin size of ~ 50 GeV appears more realistic, see the discussion below). This bin

¹³ This is based on Fig. 3 in Ref. [14], based on Ref. [79]. It should be noted that no official analysis for the experimental HL-LHC sensitivity for $\kappa_\lambda \neq 1$ is available.

Fig. 11 *Left:* Partial result σ_{interf} Eq. (15) for three different decay widths. *Right:* Effect of Γ_H^{tot} on the the invariant mass distribution for one benchmark point and three values of Γ_H^{tot} (see text)



size is used for demonstrative purposes. In a later step we will analyze the effect of different bin sizes and other experimental effects to obtain a more realistic picture of m_{hh} distributions.

4.1 General analysis of the effects

In this subsection we will analyze a toy model for the resonance to demonstrate the effects of the mass, width and couplings of the resonant Higgs boson in the s -channel exchange.

The effect of the total decay width of the heavy Higgs boson, Γ_H^{tot} , is important whenever the resonant diagram gains significance in the calculation of the cross section. This happens close to the resonance at $m_H \sim m_{hh}$, as discussed in the previous section. For a correct treatment close to the resonance the total width has to be included into the propagator,

$$\frac{1}{Q^2 - m_H^2} \rightarrow \frac{1}{Q^2 - m_H^2 + i m_H \Gamma_H^{\text{tot}}}. \quad (14)$$

From this expression one can clearly see that the dominant effect of Γ_H^{tot} appears when the intermediate Higgs boson mass is equal to the (reduced) center of mass energy Q^2 . In the Higgs pair production process, the total decay width of the heavy Higgs becomes relevant near the resonant region where the behavior of the cross section can be dominated by the interference between the resonant and the non-resonant contributions, which is proportional to

$$\sigma_{\text{interf}} = \frac{Q^2 - m_H^2}{(Q^2 - m_H^2)^2 + m_H^2 \Gamma_H^{\text{tot}2}}. \quad (15)$$

We use this expression to investigate the resonant behavior of the m_{hh} distribution. In Fig. 11 (left) we show σ_{interf} as a function of $m_{hh} = Q$. We have chosen $m_H = 300$ GeV and three exemplary values of Γ_H^{tot} : 0.1 GeV (red), 10 GeV (dark blue) and 50 GeV (light blue). In all cases σ_{interf} shows a peak-dip structure, with the change exactly at $m_{hh} = m_H$, as expected from Eq. (15). Furthermore, one observes that the highest

(smallest) peak-dip structure is obtained for the smallest (highest) value of Γ_H^{tot} , following the analytical behavior of Eq. (15). We furthermore observe that the “total width of the effect”, given by the width of the peak at half of its maximum value, increases with increasing Γ_H^{tot} , as expected.

The features observed for σ_{interf} are also found in the calculation of the m_{hh} distribution of the complete cross section, i.e. the result from taking into account the complete resonant and the non-resonant contributions, as shown in the right plot of Fig. 11. Here we depict $d\sigma/dm_{hh}$ as a function of m_{hh} for one benchmark point of benchmark **plane 4** with $m_A = m_{H^\pm} = 544.72$ GeV and $m_H = 515.5$ GeV.¹⁴ For the total width of H we find $\Gamma_H^{\text{tot}} \sim 3$ GeV, resulting in the red curve. In order to illustrate the effects of the size of Γ_H^{tot} , as seen in the left plot, we also show the results for ad-hoc set values of $\Gamma_H^{\text{tot}} = 10$ GeV (dark blue) and 50 GeV (light blue). The main features of Γ_H^{tot} (height of the peak-dip structure and the “width of the effect”) are found in the full calculation exactly as in σ_{interf} .

However, there is one important difference between the results for σ_{interf} and the full invariant mass distribution results which can be observed in Fig. 11. While for σ_{interf} a peak-dip structure is found, in the full calculation for our chosen benchmark point a dip-peak structure can be observed. This difference can be traced back to the sign of $(\lambda_{hhH} \times \xi_H^t)$, which enters as prefactor in the resonant diagram. In the left plot of Fig. 12 the resonant H diagram is shown with the two coupling factors entering the amplitude: the top-Yukawa coupling modification factor ξ_H^t of the heavy Higgs H and the THC λ_{hhH} . The right plot in Fig. 12 demonstrates the effect of $\text{sign}(\lambda_{hhH} \times \xi_H^t)$. The red curve is identical to the red curve in the right plot of Fig. 11, as obtained for the value of $\lambda_{hhH} = -0.3975$, with $\lambda_{hhH} \times \xi_H^t < 0$. The blue curve shows the m_{hh} distribution for the (ad hoc) flipped sign, i.e. with $\lambda_{hhH} = +0.3975$ (normalized to the corresponding

¹⁴ This corresponds to the green point of the model based analysis for plane 4 in the Sect. 4.3.

Fig. 12 Left: couplings involved in the resonant diagram (top Yukawa, ξ_H^t , and BSM triple Higgs coupling, λ_{hhH}). Right: invariant mass distributions for different signs of $(\lambda_{hhH} \times \xi_H^t)$

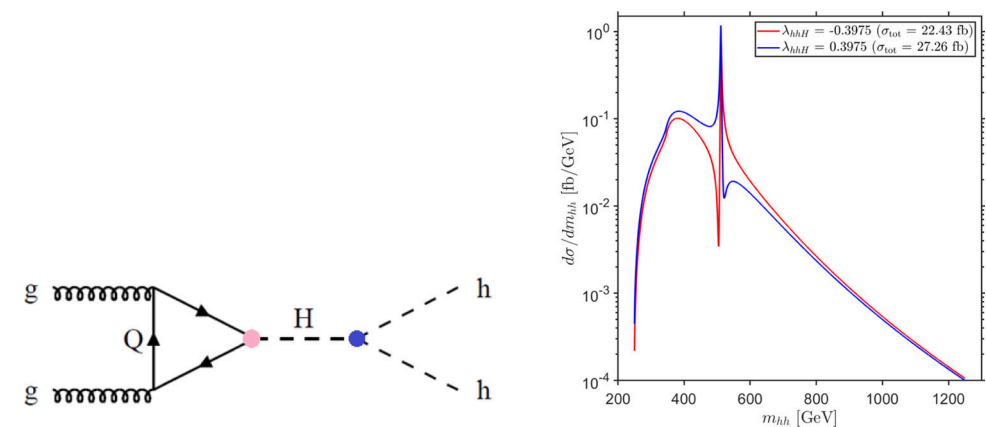


Table 2 Selected points in benchmark plane 3 with large di-Higgs production cross section

	$\tan \beta$	m_{12}^2 (GeV 2)	$c_{\beta-\alpha}$	m_H (GeV)	Γ_H^{tot} (GeV)	κ_λ	λ_{hhH}
Red	10	6801.00	-0.0735	264.75	0.09443	0.9475	-0.1505
Blue	10	8350.32	-0.0385	291.75	0.04292	0.9838	-0.0865
Black	10	6957.94	0.0140	264.75	0.02108	0.9986	0.0190

value of the full cross section obtained for this trilinear Higgs coupling). As can be expected, the flip of the sign $(\lambda_{hhH} \times \xi_H^t)$ also flips the dip-peak structure to a peak-dip structure (σ_{interf} shown above corresponds to a positive sign). The question arises whether an experimental analysis can be sensitive to the difference between peak-dip and dip-peak, and thus provide a handle on the sign of $(\lambda_{hhH} \times \xi_H^t)$. This question will be analyzed below.

4.2 Model based analysis: benchmark plane 3

We start our model based m_{hh} analysis for several points given in the benchmark plane 3. This choice is based on the fact that in this plane m_H is a free parameter, and a large variation of λ_{hhH} has been found, see the previous section. This allows for a detailed analysis of the effects of the resonant H contribution. First we will investigate the points that present the largest enhancement of the cross section w.r.t. the SM within the allowed region, as listed in Table 2. Second we will look at points with $c_{\beta-\alpha} \sim 0.1$, as listed in Table 4. Finally we will analyze points with $c_{\beta-\alpha} \sim 0.2$, i.e. a relatively large deviation from the alignment limit, as listed in Table 5. The aim of this study is to extract the general behavior and the influence of specific parameters on the experimental measurement of the cross section. This will allow us to track variations of the parameters that we are mostly interested in (m_H , Γ_H^{tot} and λ_{hhH}).

4.2.1 Benchmark plane 3: large di-Higgs production cross sections

We first analyze three points in benchmark plane 3 with large enhancements of the di-Higgs production cross section w.r.t.

the SM. They are located close to the alignment limit and can be seen in the left part of Fig. 13 as red, blue and black dots. In the first step of the analyses we choose a bin size of 5 GeV to make the large resonant enhancement, which is very narrow, clearly visible. The values of the parameters of each point are listed in Table 2.

The di-Higgs production process is kinematically forbidden for $m_{hh} < 250 \text{ GeV} = 2m_h$. Once this threshold is surpassed, one can observe a resonant enhancement for $m_{hh} \sim m_H$. This is clearly seen at the location of the resonant peaks in the invariant mass distribution in Fig. 13 (middle). For the red and the black points the resonant peak is found around $\sim 265 \text{ GeV}$, while for the blue point it is located at $\sim 292 \text{ GeV}$, corresponding to the respective m_H value. The “height” and “width” of the peaks is related to the total decay width Γ_H^{tot} of the heavy Higgs boson, which is largest for the red point ($\sigma/\sigma_{\text{SM}} \sim 8$) and smallest for the black point ($\sigma/\sigma_{\text{SM}} \sim 2.5$), as shown in Table 2. Furthermore, the resonant heavy Higgs contribution yields the already observed typical pattern, a peak-dip or dip-peak structure, depending on the parameter point. The peak-dip structure is observed in the blue and red points, whereas in the case of the black point one can only see the peak, see the discussion below. This pattern is clear when looking at the zoom in the low m_{hh} region in the right plot of Fig. 13. Moreover, we observe for all three points an enhancement at an invariant mass of 350–400 GeV, which is related to the top pair production threshold in the resonant diagram.¹⁵

The three points have different values of $c_{\beta-\alpha}$, which change the Yukawa coupling of the top quark according to

¹⁵ The mass of the top quark used in the calculation is $m_t = 173.2 \text{ GeV}$, therefore $2m_t = 346.4 \text{ GeV}$.

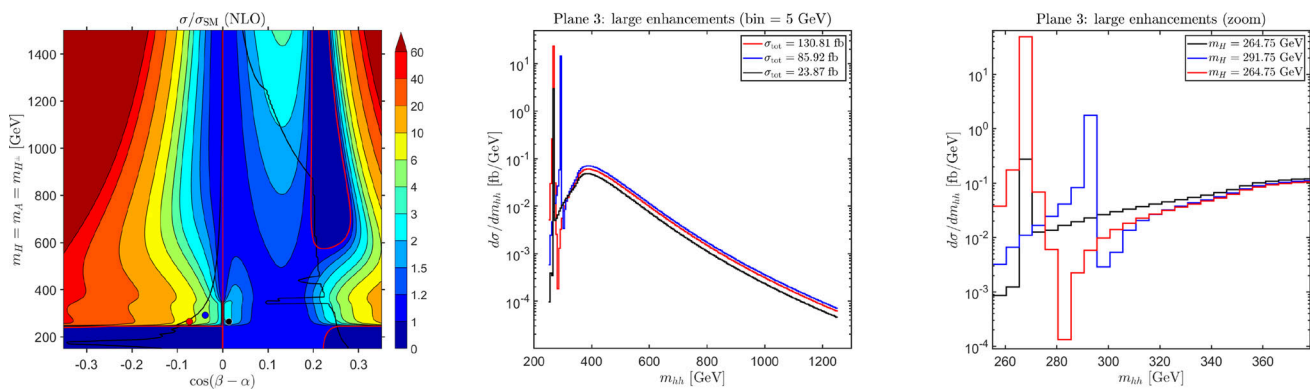


Fig. 13 Analysis of points with large di-Higgs production cross sections in the benchmark plane 3. Left: location of the benchmark points in the total production cross section plot. Middle: invariant mass distribution for selected points (with a bin size of 5 GeV). The colors of the

points in the two figures are matching. The values of σ_{tot} in the legend indicate the LO inclusive cross section prediction for each point. Right: zoom in the region of interest in the m_{hh} distribution

Table 3 Structure of the resonance

	λ_{hhH}	ξ_H^t	sign	structure
Red	-0.1505	-0.1738	+	Peak-dip
Blue	-0.0865	-0.1384	+	Peak-dip
Black	0.0190	-0.0810	-	Dip-peak

the expression:

$$\xi_H^t = c_{\beta-\alpha} - s_{\beta-\alpha} \cot \beta, \quad (16)$$

resulting in a positive (negative) sign of $(\lambda_{hhH} \times \xi_H^t)$ for the red and blue (black) points, as shown in Table 1. This in turn results in a peak-dip (dip-peak) structure, cf. Table 3. The pattern of the differential distribution changes according to the sign of $(\lambda_{hhH} \times \xi_H^t)$. For the black curve only a peak is visible, because the dip before it cannot be produced for masses below 250 GeV.

A more detailed analysis of the three points is presented in Fig. 14, where we analyze the contribution of individual (groups of) diagrams. In the upper left plot we show the total, i.e. including all diagrams, distribution for the three points (as in the right plot of Fig. 13) but changing the bin size to 20 GeV in order to represent a more realistic experimental set up. One can observe already in the example of the black point that the bin size (and location) is important for the observation of the phenomenological features, as the closeness to the kinematic threshold can prevent the dip-peak structure to develop fully in the observed distribution.

In the upper right, and lower row of Fig. 14 we disentangle the contributions of the individual diagrams for the red, black and blue points, respectively. We have calculated the total differential distribution including all three diagrams for di-Higgs production (red), the SM-like cross section, called

continuum, – including only the box and the SM-like Higgs boson in the s -channel diagrams – (black), the contribution of the diagram with no triple Higgs couplings involved, i.e. the box diagram (yellow), the contribution of the two diagrams with the triple Higgs couplings, which includes the h and H in the s -channel (purple), and the contribution with only h (light blue) and with only H (dark blue), respectively, in the s -channel. For all three points the same pattern can be observed. The 2HDM cross section (red) follows largely the SM-like distribution (black), apart from the strong resonant enhancement at $m_{hh} \sim m_H$. This is caused by the H s -channel contribution (blue), potentially providing sensitivity to λ_{hhH} . Furthermore, the destructive interference of the box-diagram (yellow) and the SM-like h -exchange contribution (light blue) is clearly visible in the continuum, i.e. SM-like, contribution of the distribution (black).

4.2.2 Plane 3: $c_{\beta-\alpha} \sim 0.1$

Next we proceed to study a set of points that are all located at the same value of $c_{\beta-\alpha} \sim 0.1$. The exact value of $c_{\beta-\alpha} = 0.1015$ results from the grid used to scan this plane. In this case the only change between the benchmark points, as listed in Table 4, is the common mass m_H of the heavy Higgses, with correspondingly modified couplings and decay widths.

The points are also shown as orange, yellow, purple, garnet and green dots (in ascending mass order) in the upper left plot of Fig. 15 (repeating the upper left plot of Fig. 8). The upper right plot of Fig. 15 (repeating the middle right plot of Fig. 9) indicates the location of these points in the κ_λ - λ_{hhH} plane. One can observe that with increasing m_H the points are decreasing in κ_λ (from $\kappa_\lambda \sim 1$ down to zero) and are increasing in λ_{hhH} (from λ_{hhH} close to zero to $\lambda_{hhH} \sim 1$).

The m_{hh} distributions for the five benchmark points are presented in the lower plot of Fig. 15, with a bin size of

Fig. 14 m_{hh} distributions for selected points in plane 3. Upper left: total m_{hh} distributions for the points of Table 2; upper right (red), lower left (blue), lower right (black): individual contributions to the m_{hh} distribution for the three points: total cross section (red), continuum cross section (black), m_{hh} involving only λ_{hhh} (λ_{hhH}) in light (dark) blue, m_{hh} involving both (no) THCs in purple (yellow)

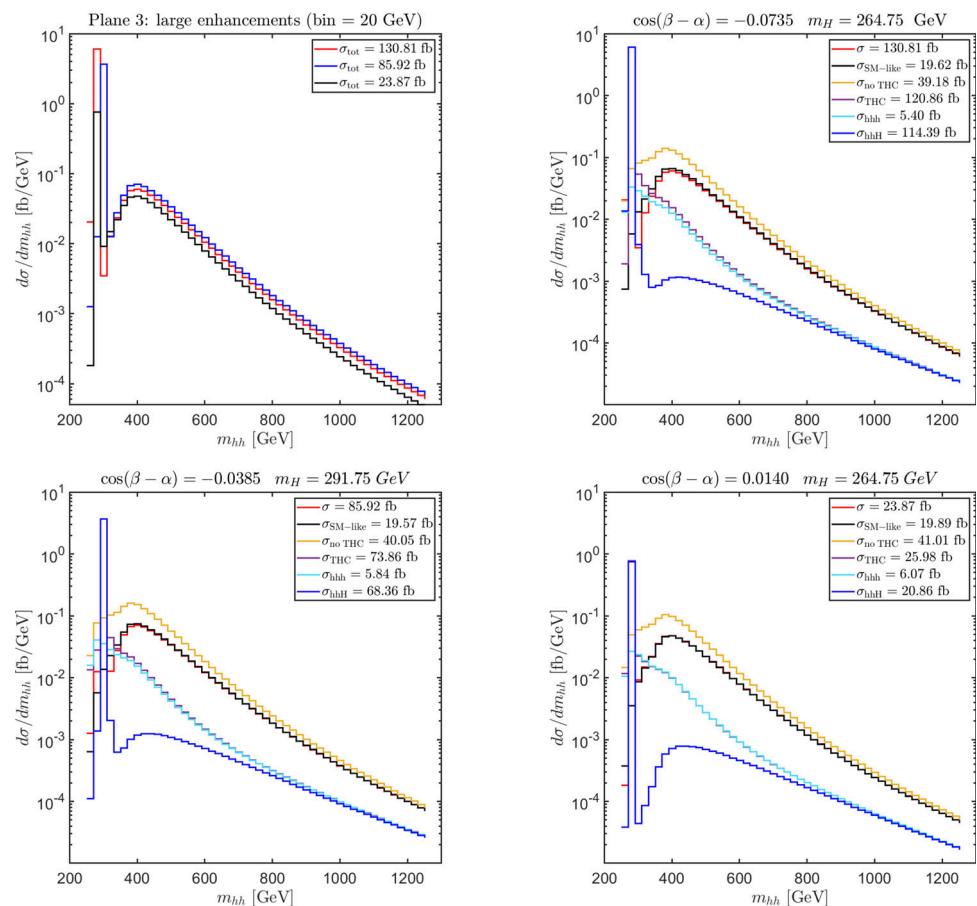


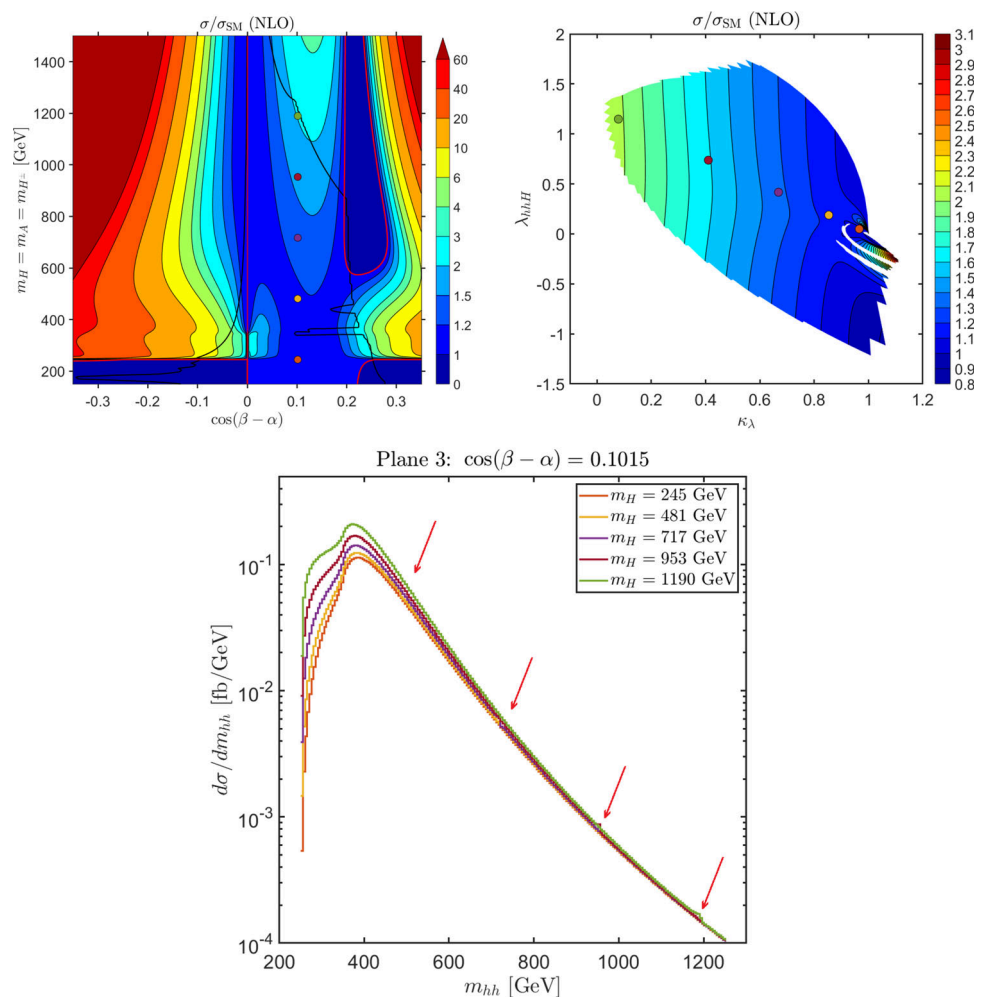
Table 4 Selected points in benchmark **plane 3** for $c_{\beta-\alpha} \sim 0.1$

	$\tan \beta$	m_{12}^2 (GeV 2)	α	m_H (GeV)	Γ_H^{tot} (GeV)	κ_λ	λ_{hhH}
Orange	10	5978.00	0.00201	244.50	0.03648	0.9658	0.0490
Yellow	10	23111.96	0.00201	480.75	0.61080	0.8536	0.1880
Purple	10	51408.69	0.00201	717.00	2.2380	0.6684	0.4175
Garnet	10	90868.19	0.00201	953.25	5.4440	0.3338	0.5481
Green	10	141490.45	0.00201	1189.5	10.750	-0.0397	0.8501

5 GeV. The color indicates the value of m_H (as defined in the upper plots). The red arrows indicate the location of the “resonant peaks” (for $m_H > 250$ GeV). The resonant enhancement is found to be tiny, despite the non-negligible values of λ_{hhH} . The reason for the unrealistically small bin size of 5 GeV is to see any peak at all. It is clear that for these points the enhancement of σ_{HDM} w.r.t. σ_{SM} is caused purely by the reduced κ_λ values which alleviates the destructive interference between triangle and box contributions present in the SM. The resonant H exchange hardly contributes to the total cross section. The structure of the enhancement in this case is hard to infer from the plot, but looking closely one can see a peak-dip structure. The reason for this small resonant contribution can be found in the top Yukawa coupling value of the heavy \mathcal{CP} -even Higgs. Following Eq. (16) we obtain a value

of $\xi_H^t = 5 \times 10^{-4} > 0$, thus rendering the resonant contribution negligible. The triple Higgs couplings λ_{hhH} listed in Table 4 are all positive, so that the overall sign for the coupling factor of the triangle contribution is positive and the (hardly visible) structure is a peak-dip one as expected. Furthermore, we have seen in Fig. 14 that the largest contribution in the lower mass spectrum comes from the diagram with a light Higgs h exchange, i.e. from the diagram involving κ_λ . This diagram hence drives the behavior of the distribution. In the lower plot of Fig. 15 this trend is clearly visible in the lower part of the spectrum, $m_{hh} \lesssim 350$ GeV. The smaller the value of κ_λ for a particular point (as seen in upper right plot), the larger the enhancement in the invariant mass distribution at lower m_{hh} . The most extreme point is the green one, for which κ_λ is close to zero, and the m_{hh} spectrum shows a clear

Fig. 15 Sensitivity to triple Higgs couplings for points with $c_{\beta-\alpha} = 0.1015$ in benchmark plane 3. Upper left: the common mass $m \equiv m_H = m_A = m_{H^\pm}$ and correspondingly m_{12}^2 change, as marked with orange, yellow, purple, garnet and green dots (in ascending mass order, color coding indicating $\sigma/\sigma_{\text{SM}}$). Upper right: location of the benchmark points in the κ_λ - λ_{hhH} plane (color coding indicating $\sigma/\sigma_{\text{SM}}$). Lower plot: m_{hh} distribution for the five benchmark points with a 5 GeV bin size. The colors indicate m_H , the red arrows show the location of the “resonant peak”



bump at $m_{hh} \sim 350$ GeV. It should be recalled that the gluon fusion di-Higgs production cross section has a minimum for $\kappa_\lambda \sim 2.5$ and is higher for small (or very large values) of κ_λ .

4.2.3 Plane 3: $c_{\beta-\alpha} \sim 0.2$

We finish our analysis of benchmark points in plane 3 with five points with a relatively large value of $c_{\beta-\alpha} \sim 0.2$, i.e. relatively far away from the alignment limit, as given in Table 5. As above, the exact value of $c_{\beta-\alpha} = 0.203$ is given by the scanned grid. The points are shown in the upper left and upper right plot of Fig. 16 as colored dots in orange, yellow, purple, garnet and green dots (in ascending mass order), color coding indicating $\sigma/\sigma_{\text{SM}}$ in the $c_{\beta-\alpha}$ - m_H and κ_λ - λ_{hhH} plane in the upper left and right plot, respectively. As can be observed in the upper right plot, all points have $\kappa_\lambda \sim 1$, i.e. no relevant change in the cross section can be expected from the contribution of the h -exchange diagram, so the lower part of the m_{hh} spectrum is very similar for all the points. On the other hand, the values of λ_{hhH} decrease from around zero down to $\lambda_{hhH} \sim -0.5$. However, as can be seen in the two upper plots of Fig. 16, the variation of the total cross section

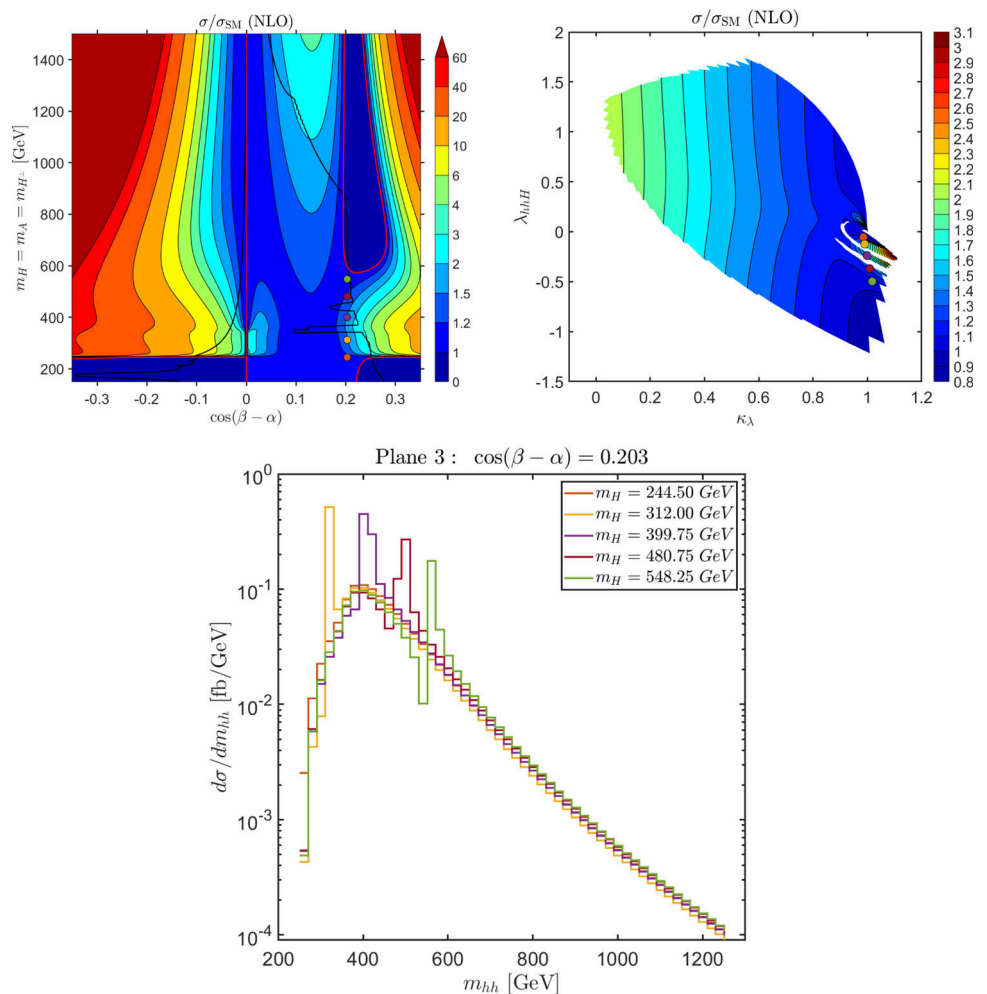
is relatively small. The largest cross sections are found for $m_H = 312.0$ GeV (yellow) and $m_H = 399.75$ GeV (purple), i.e. around ~ 350 GeV, see the discussion in Sect. 4.2.1. In the lower plot of Fig. 16 we show the m_{hh} distribution for the five points. For four of them with $m_H > 2m_h$ a clear resonance dip-peak structure can be observed at $m_H \sim m_{hh}$, as expected.

In Fig. 17 we present a more detailed analysis of the sensitivity to the triple Higgs couplings in the invariant mass distribution following the same notation as in Fig. 14. We show the invariant mass distribution from all the diagrams in the upper right plot and then split the individual contributions for each particular mass point in the rest of the plots. The first one for $m_H = 244.5$ GeV is shown in the upper middle plot, which has m_H below the di-Higgs production threshold. Consequently, no enhancement due to the diagram containing λ_{hhH} can be observed, and the total cross section is almost indistinguishable from the SM-like result in this case. For the other masses we find a similar result as in Fig. 14. One can observe that the s -channel contribution involving the heavy Higgs with its trilinear coupling λ_{hhH} is responsible for the enhancement close to the mass of the intermediate Higgs

Table 5 Selected points in benchmark plane 3 for $c_{\beta-\alpha} \sim 0.2$

	$\tan \beta$	m_{12}^2 (GeV ²)	α	m_H (GeV)	Γ_H^{tot} (GeV)	κ_λ	λ_{hhH}
Orange	10	5912.66	0.10475	244.50	0.146	0.9851	-0.0549
Yellow	10	9627.97	0.10475	312.00	0.463	0.9902	-0.1240
Purple	10	15805.30	0.10475	399.75	1.291	0.9864	-0.2388
Garnet	10	22859.37	0.10475	489.75	2.550	1.0083	-0.3699
Green	10	29729.19	0.10475	548.25	3.995	1.0177	-0.4977

Fig. 16 Sensitivity to triple Higgs couplings for points with $c_{\beta-\alpha} = 0.203$ in benchmark plane 3. Upper left: $m \equiv m_H = m_A = m_{H^\pm}$ and correspondingly m_{12}^2 changes, as marked with orange, yellow, purple, garnet and green dots (in ascending mass order, color coding indicating $\sigma/\sigma_{\text{SM}}$). Upper right: location of the benchmark points in the κ_λ - λ_{hhH} plane (color coding indicating $\sigma/\sigma_{\text{SM}}$). Lower plot: m_{hh} distribution for the five benchmark points. The colors indicate m_H



boson, while the effect of the κ_λ is mostly significant in the low mass region of the plot. The contribution of the diagrams involving THCs (purple) interferes with the continuum (box diagram) shown in yellow and creates the dip-peak structure that can be observed in the total distributions, see Fig. 17 (upper left).

The top Yukawa coupling for this value of $c_{\beta-\alpha}$ is $\xi_H^t = 0.1020 > 0$, and thus the sign of $(\lambda_{hhH} \times \xi_H^t)$ is negative, resulting in the dip-peak structure observed. In principle, this type of distributions can yield a handle on the size and sign of λ_{hhH} , as will be discussed in more detail below.

In Fig. 18 we further analyze the interference contributions of the s -channel diagrams in Fig. 1. In the left plot we show the interference term of the diagram with the s -

channel h exchange (A) and diagram with the s -channel H exchange (B). The interference term in this case is defined as $|A + B|^2 - |A|^2 - |B|^2$. The solid (dashed) lines indicate positive (negative) interference. One can observe a similar behavior to the above discussed interference between resonant and box contributions, i.e. that these two diagrams interfere constructively up to $m_{hh} \leq m_H$, and destructively for larger m_{hh} values, i.e. the interference term changes its sign. The diagram A and the box diagram (C) interfere negatively across the whole invariant mass range as shown in the middle plot of Fig. 18. This behavior corresponds to the result found for the SM di-Higgs production, where only these two diagrams are present. Finally, the interference of B and C, shown in the right plot of Fig. 18, has two sign changes. Up

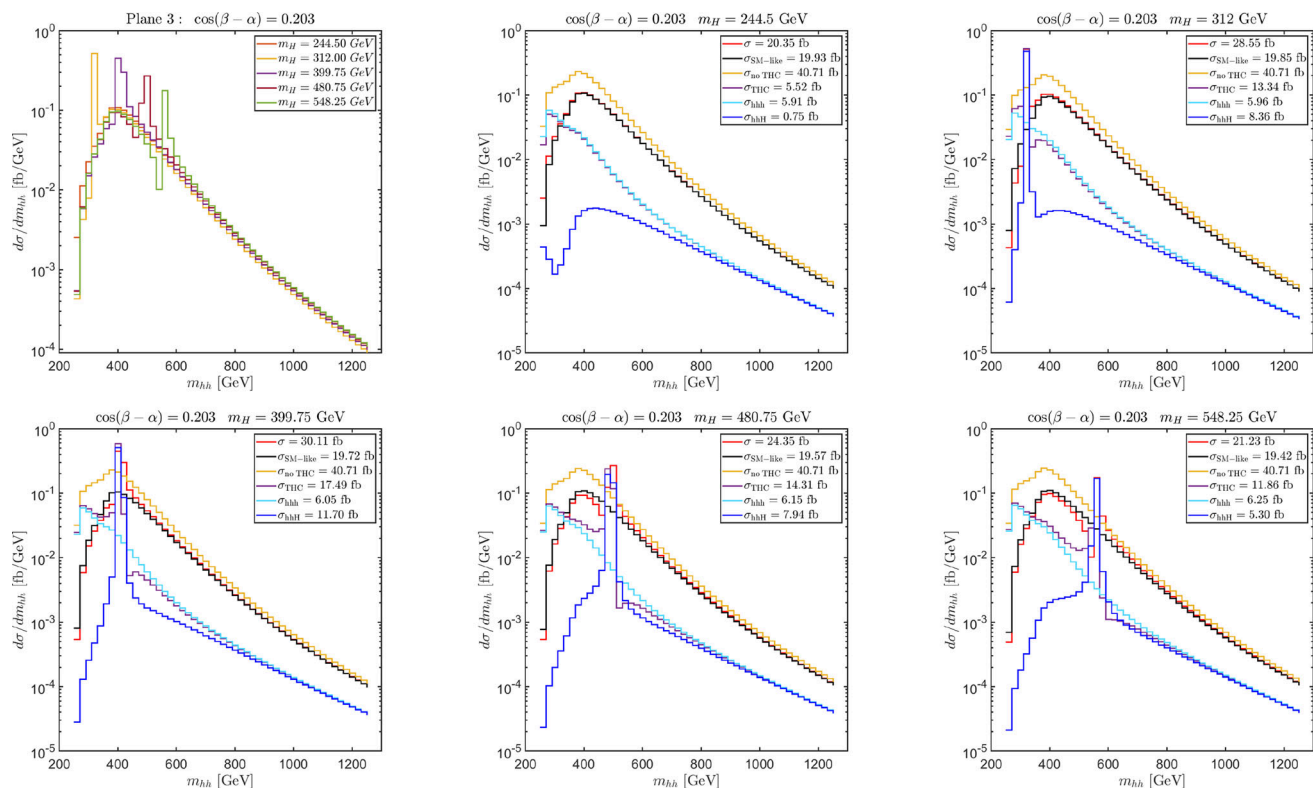


Fig. 17 m_{hh} distributions for selected points in plane 3 with $c_{\beta-\alpha} \sim 0.2$. Upper left: total m_{hh} distributions for the points of Table 5; upper middle, left and lower left, middle and right: individual contributions

to the m_{hh} distribution for the five points: total SM-like cross section in black, total cross section in red, m_{hh} involving only λ_{hhh} (λ_{hhH}) in light (dark) blue, m_{hh} involving both (no) THC in purple (yellow)

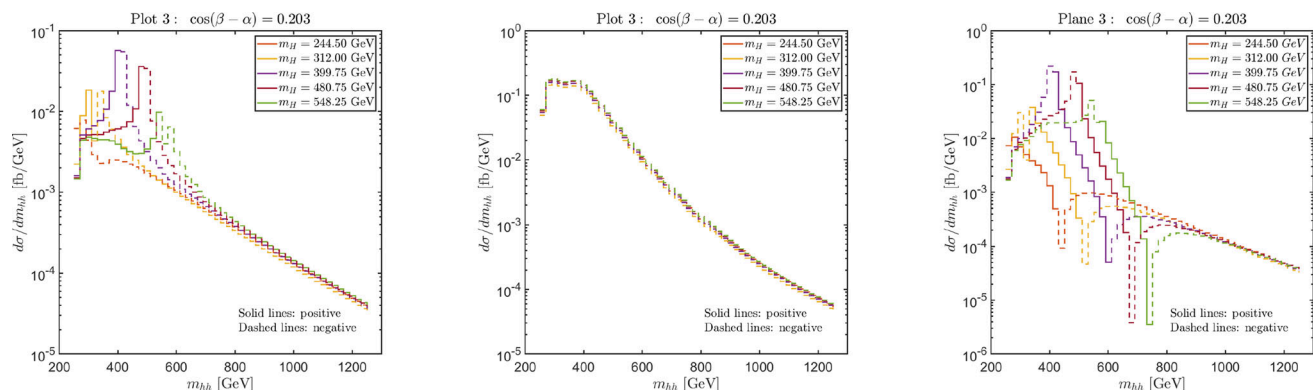


Fig. 18 Interference contributions for the benchmark points in plane 3 with $c_{\beta-\alpha} = 0.203$. Left: interference of the two triangle diagrams. Middle: interference of the SM-like diagrams. Right: interference between

the box and the resonant diagram. Solid lines indicate that the interference is positive and dashed lines indicate that it is negative

to $m_{hh} \leq m_H$ the interference is negative, leading to the dip in the total m_{hh} distribution. For larger values it turns positive, leading the subsequent peak in the total distribution, see the discussion in Sect. 4.1. The second sign change happens because the interference approaches zero at an m_{hh} value not related to m_H . In the plot the interference lines in principle

go down to zero, which, however, is not visible due to the log scale and the finite bin width.

4.3 Model based analysis: benchmark plane 4

To complete our m_{hh} analysis we investigate benchmark points in plane 4. In this plane the heavy Higgs boson masses,

Table 6 Selected points in benchmark plane 4 for $m_A = m_{H^\pm} \sim 545$ GeV

	$\tan \beta$	m_{12}^2 (GeV ²)	$c_{\beta-\alpha}$	m_H (GeV)	Γ_H^{tot} (GeV)	κ_λ	λ_{hhH}
Purple	10	4899.61	0.2	222.50	0.09306	0.9816	-0.0321
Orange	10	8612.82	0.2	295.00	0.3464	0.9835	-0.0964
Blue	10	13366.45	0.2	367.50	0.8694	0.9860	-0.1788
Light blue	10	19160.49	0.2	440.00	1.7540	0.9891	-0.2791
Green	10	25994.95	0.2	512.50	3.0020	0.9927	-0.3975
Yellow	10	33869.83	0.2	585.00	4.6720	0.9968	-0.5339
Garnet	10	42785.13	0.2	657.50	9.2810	1.0015	-0.6883

as in plane 3, are free parameters and are in agreement with the applied constraints over a relatively large interval, i.e. the effects of a mass variation (as well as a variation of λ_{hhH}) can be readily analyzed. In contrast to plane 3, however, we are always far away from the alignment limit by fixing $c_{\beta-\alpha} = 0.2$. Furthermore, the effects of a variation of m_H can be better isolated by defining this mass independent of the other heavy BSM Higgs-boson masses. The selected points are listed in Table 6. They are all located at the same mass of $m_A = m_{H^\pm} = 544.75$ GeV. As was demonstrated in Sect. 3.3, κ_λ and λ_{hhH} are proportional to each other, and allowed values of λ_{hhh} are within $\sim 2\%$ of $\kappa_\lambda = 1$, whereas λ_{hhH} is found for our benchmark points in the interval $[\sim 0, -0.7]$. Similarly, also Γ_H^{tot} grows with increasing m_H . All corresponding numerical values can be found in Table 6.

The location of the points in the benchmark plane is shown in the upper left plot of Fig. 19, and in the κ_λ - λ_{hhH} plane in the upper right plot. The lower row shows the corresponding m_{hh} distributions with the color indicating the m_H value. In the left plot, for better visibility, we show the idealized case of a bin size of 5 GeV, whereas the right plot shows the more realistic case of 20 GeV.

One can observe that the resonant structure in this case is dip-peak since (as in the previous case) the top Yukawa coupling is positive and the BSM THC is negative. For the purple point no enhancement can be observed, since its mass is below the di-Higgs production threshold, $m_H^{\text{purple}} = 222.5$ GeV. The remaining points show a resonant enhancement as the invariant mass approaches the mass of the heavy Higgs, i.e. one expects to have the highest sensitivity to the THC λ_{hhH} in this region. The difference between the heights of the peaks is found to be largest for small m_H , but naturally also decreases with increasing bin size, which will be further discussed below. The increasing bin size, in particular, decreases the visibility of the dip, an effect that is in particular visible for low m_H . This demonstrates the relevance of the bin size in a realistic experimental analysis (and will also be further discussed below).

5 Impact of experimental uncertainties

In this section we will analyze the impact of experimental uncertainties on the possible sensitivity to λ_{hhH} . These effects are the experimental smearing, i.e. the uncertainty in the m_{hh} measurement, the experimental resolution, i.e. the size of the bin width, as well as the arbitrary location of the bin. We will also demonstrate how the experimental results for λ_{hhH} change with a variation of $\text{sign}(\lambda_{hhH} \times \xi_H^t)$. We neglect any “background” from other SM processes. This would be subject to an dedicated experimental analysis that is far beyond the scope of our paper.

In order to estimate the sensitivity to the BSM coupling λ_{hhH} , following Ref. [22], we define a theoretical quantity that aims to quantify the “sensitivity to λ_{hhH} ” (but is not meant as a determination of its precision, which requires a detailed experimental analysis, which is beyond the scope of our paper). We define

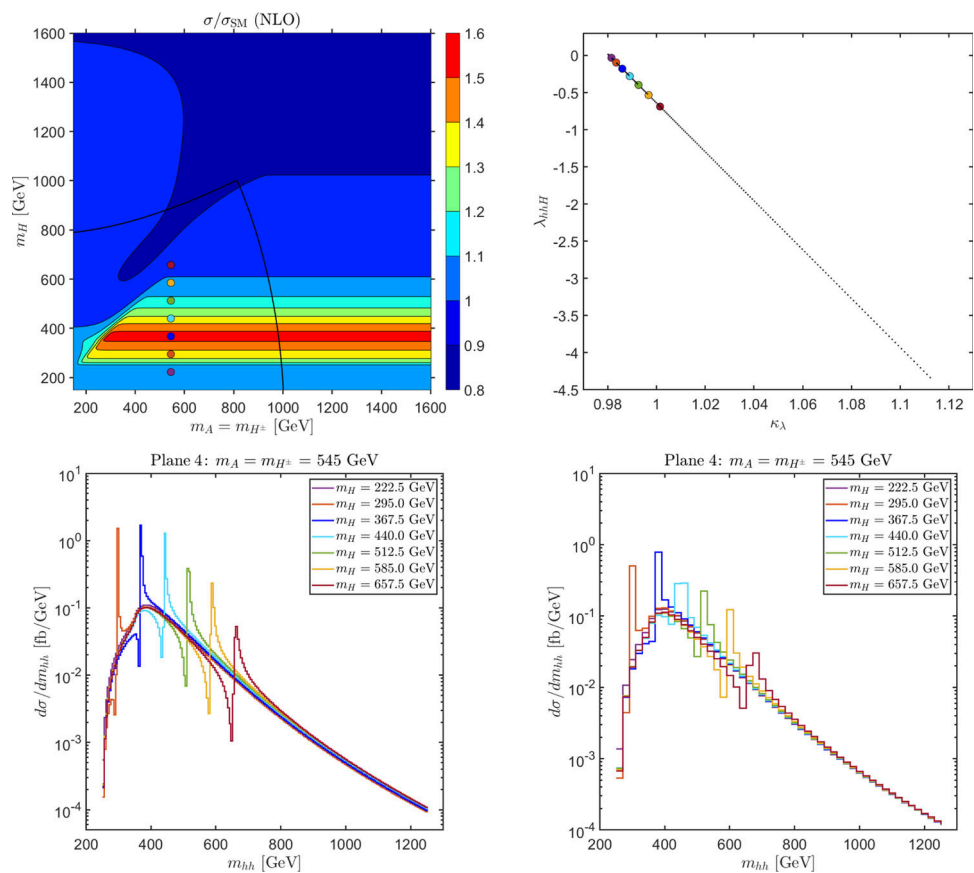
$$R := \frac{\sum_i |N_i^R - N_i^C|}{\sqrt{\sum_i N_i^C}}, \quad (17)$$

where N^R is the number of events of the resonant contribution, and N^C is the number of events of the continuum. The window in which the events are counted is defined by

$$|N^R - N^C| > \text{bin size} \times 20 \text{ GeV}. \quad (18)$$

The sum over i in Eq. (17) runs over all the bins that fulfill this condition. The chosen condition in Eq. (18) starts with a minimum of 1000 excess events due to the resonance when the bin size is 50 GeV and 200 events when the bin size is 10 GeV, i.e. smaller bin sizes are not “punished”. Using the absolute value in the definition of R in Eq. (17), as well as in the definition of the window in Eq. (18) effectively makes use of both the dip and the peak of the smeared distribution. This constitutes a simplified theory definition, where in a realistic experimental analysis the dip-peak structure would be taken into account via a template fitting, see e.g. the analysis in Ref. [80]. The numbers of events are in turn obtained using the relation between the cross section and the integrated

Fig. 19 Sensitivity to triple Higgs couplings for points within benchmark plane 4. Upper left: the points have fixed $m_A = m_{H^\pm} = 544.75$ GeV, $c_{\beta-\alpha} = 0.2$, whereas m_H and correspondingly m_{12}^2 change, as marked with purple, orange, blue, light blue, green, yellow and garnet dots (in ascending mass order, color coding indicating $\sigma/\sigma_{\text{SM}}$). Upper right: location of the benchmark points in the κ_λ - λ_{hhH} plane. Lower line: m_{hh} distribution for the seven benchmark points with a bin size of 5 (20) GeV in the left (right) plot. The colors indicate m_H



luminosity of the collider,

$$N = \sigma \cdot \mathcal{L}, \quad (19)$$

where we have used $\mathcal{L} = 6000 \text{ fb}^{-1}$, i.e. the sum of the anticipated luminosity of ATLAS and CMS combined at the end of the HL-LHC run. This constitutes the most optimistic case.

5.1 Smearing

Differential cross section measurements are affected by the finite resolution of the detectors. This translates into a blurred or “smeared” spectrum that can be observed in such experiments. We try to mimic this effect by artificially smearing the theoretical prediction for the invariant mass distributions of the chosen benchmark points. To do this we introduce a statistical error to our prediction of the invariant mass. We apply the uncertainties in m_{hh} by allowing the value of an event to shift to the left or to the right in the spectrum according to a Gaussian probability distribution. The amount of smearing is defined in terms of a percentage of smearing p that indicates that the predicted value x should stay within the interval $[(1-p) \cdot x, (1+p) \cdot x]$ with a 78% probability, which corresponds to the definition of the full width half maximum

of the Gaussian distribution (as given for the experimental analyses).

We illustrate this effect in Fig. 20 for one particular example of a benchmark point taken from the benchmark plane 4 with the masses fixed to $m_A = m_{H^\pm} = 544.72$ GeV and $m_H = 515.5$ GeV.¹⁶ In this figure we show in blue the m_{hh} distribution without smearing (the ideal case). The solid line depicts the full distribution, whereas the dashed line shows the result for the continuum (non-resonant) diagrams. The red lines demonstrate the effect of applying a 10% (left plot) and 15% (right plot) smearing on the theoretical prediction of the m_{hh} distributions, where the solid (dashed) lines indicates the full (continuum) result. While a 15% smearing was given as a realistic future estimate, the 10% smearing indicates a potential optimistic improvement. One can observe that from the original dip-peak structure as seen in the solid blue line effectively only a peak or bump around the original peak remains. The original dip is visible only as a very small reduction of the unsmeared distribution, as the relative weight of the points below the continuum is smaller than those above the continuum (note the logarithmic scale). Furthermore it should be noted that on the edges of the m_{hh} values there is a slight bump in the smeared distribution. This

¹⁶ This corresponds to the green point of the model based analysis for plane 4 in Sect. 4.3, which is also the point used in Sect. 4.1.

Fig. 20 Theoretical (blue) and smeared (red) invariant mass distributions for the selected benchmark point (see text). Solid (dashed) lines show the contribution of the total (continuum) differential cross section. Left (right) plot has a 10% (15%) smearing

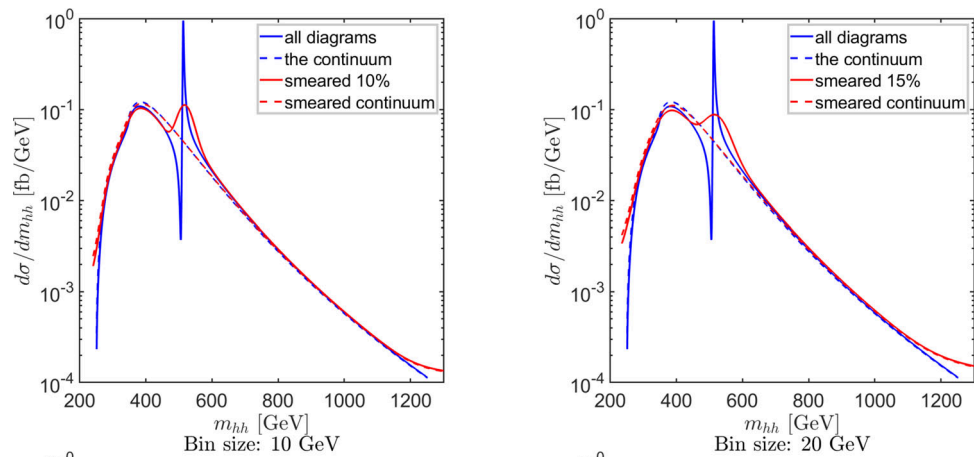
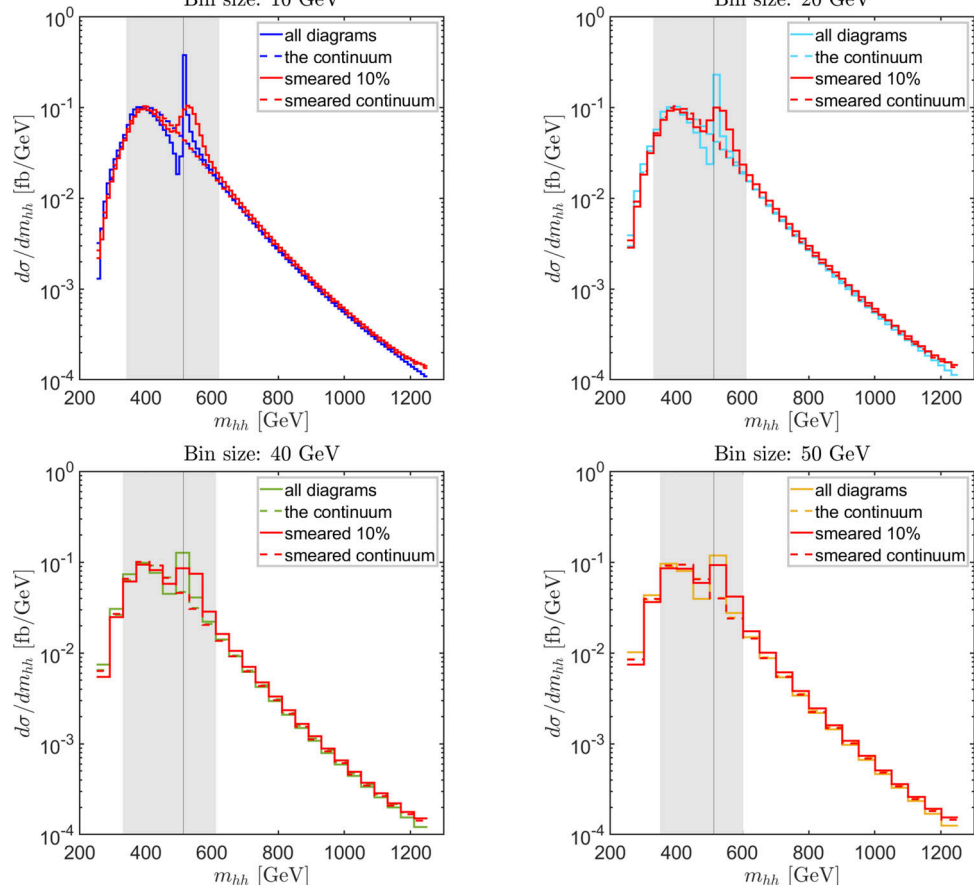


Fig. 21 Different bin sizes for a 10% smeared distribution in the example benchmark point (10, 20, 40 and 50 GeV). The red lines correspond to the true (smeared and binned) prediction of the m_{hh} distribution. The other color indicates the corresponding binned, but unsmeared distribution. Solid (dashed) lines represent the total (continuum) contribution to the cross section. The grey region represents the region that falls into the window defined to compute the variable R . The black vertical line indicates the value of the resonant mass, i.e. 512.5 GeV



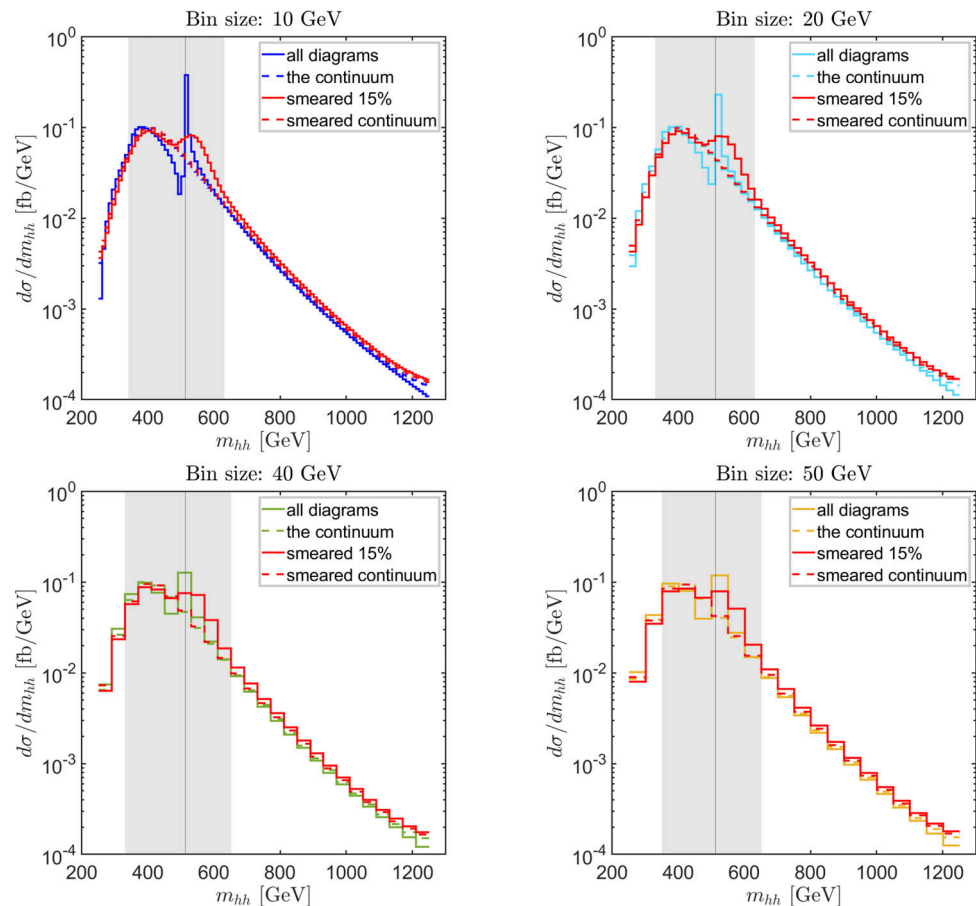
is an artifact of the method that we used for the smearing and should be neglected. Since we do not generate the number of events but rather a theoretical prediction for a specific value of $d\sigma/dm_{hh}$, we cannot redistribute the events according to some uncertainty. What we do is an approach that is independent of the number of events but should be equivalent. We generate a Gaussian probability distribution function centered at each of the predicted points and a standard deviation according to the percentage of smearing as explained above. Afterwards at each point in m_{hh} the gaussians of the full distribution are summed and finally normalized to the original value of the integrated total cross section. This corresponds

to taking the limit of the number of events $N \rightarrow \infty$. At the edges only events from one side contribute to the sum of the gaussians and are not lowered by a smaller counterpart on the other side. If the distribution would continue down to infinite values, there would be no bumps at the edges.

5.2 Bin width

As a further step in the evaluation of the experimental challenges, we analyze the effect of the bin width. The binning means that the data in a particular interval in m_{hh} is presented as the mean value of the differential cross section of

Fig. 22 Same as Fig. 21 but for 15% smearing



all the points that fall in that interval. Assuming that at least one of the Higgs bosons analyzed will decay in a $b\bar{b}$ pair,¹⁷ the bin size will eventually be determined by the b -jet mass resolution from the reconstruction of the $h \rightarrow b\bar{b}$ decay mode. This affects the visualization of the results in a realistic experimental set up, but also the counting of events for the evaluation of the experimental sensitivity, see Eq. (17). The binning is applied after the smearing discussed in the previous subsection.

The analysis is performed for the same benchmark point as in Sect. 5.1. In Figs. 21 and 22 we show the same spectrum but for a different bin size in the m_{hh} variable: 10 GeV (upper left), 20 GeV (upper right), 40 GeV (lower left) and 50 GeV (lower right). Figure 21 assumes a 10% smearing, whereas in Fig. 22 we show the more realistic result with 15% smearing. The red lines show the true (smeared and binned) prediction, whereas the other colors indicate the unsmeared, but binned results for comparison. One can observe that the effect of the smearing becomes less significant in the region of resonant production for a larger bin size. The resonance is already partially diluted by the smearing, and the effect of the binning becomes less visible, as can be observed best in the lower

Table 7 Values of the variable R for the significance of the signal for different bin sizes for a 10% and 15% smeared distribution, see Figs. 21 and 22

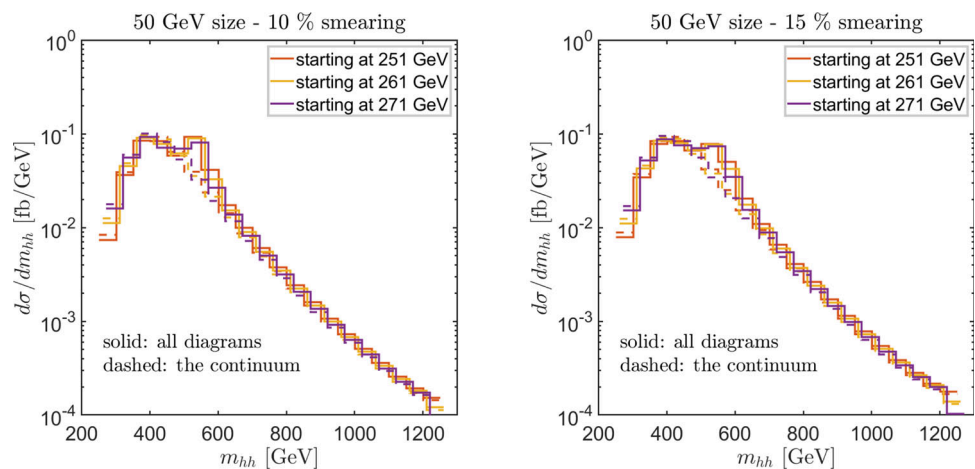
Bin size	R (10% smear)	R (15% smear)
10 GeV (blue)	94.7	84.9
20 GeV (light blue)	92.6	86.5
40 GeV (green)	92.6	86.8
50 GeV (yellow)	89.6	87.5

right plots of Figs. 21 and 22. The effect of the binning is less important once the smearing of the experimental data is taken into account. After the binning the “dip” is effectively indistinguishable from the continuum contribution. The peak is still persistent and for larger bin size approaches the same height as the bump at ~ 400 GeV before binning.

In the most conservative result the expected experimental resolution should have a bin size of 50 GeV and a smearing of $\sim 15\%$. The expected results in this case would possibly give access to the location of the resonance (the mass of the \mathcal{CP} -even H should be known via single production by the time the di-Higgs cross section is measured) and partially to the height, and thus possibly to the size of λ_{hhH} . In order to make a quantitative estimate of the sensitivity of the signal produced by the resonant diagram we have calculated the

¹⁷ The most promising decay mode for the other Higgs is $\gamma\gamma$ because of the excellent di-photon mass resolution.

Fig. 23 Invariant mass distributions for different bin locations assuming a bin size of 50 GeV and a smearing of 10% (left) and 15% (right). Solid (dashed) curves show the full (continuum) result



value of the variable R defined in Eq. (17) that is obtained from Figs. 21 and 22, shown in Table 7. The grey region represents the region that falls into the window defined to compute the variable R . Overall, one can see that the values of R are significant, i.e. the signal could possibly be distinguished at the HL-LHC if our assumptions on the experimental uncertainties are met. It should be noted that we are not taking into account the efficiency of the particle detectors, which could reduce significantly the estimate of R . Comparing the two columns in Table 7 one observes R is roughly 10% worse as the assumed percentage of smearing increases by 5%. However, R is somewhat more stable w.r.t. the bin size, where deviations within $\sim 5\%$ are found. This would constitute a rather positive feature for an experimental set-up.

5.3 Bin location

The next part of the analysis concerns the arbitrary choice of the location of the bin. This choice can also affect the pattern of the invariant mass distribution. The concrete value of m_{hh}^{\min} (the value of m_{hh} at the bin start) and m_{hh}^{\max} (the value of m_{hh} at the bin end) affects the number of events that fall into that bin and thus can have an impact on the evaluation of the sensitivity R . For the previously used benchmark point we change the location of the bin for a 10% and 15% smeared distribution and a 50 GeV bin size.

In Fig. 23 we show the difference in the invariant mass distribution created by a change in the location of the first bin by 10 or 20 GeV, i.e. we start the distribution at 251, 261, 271 GeV as orange, yellow and purple lines, respectively. In both plots we show the difference between the total differential cross section (solid lines) and the continuum contribution (dashed lines). The left (right) plot uses a smearing of 10% (15%). One can observe that for all three choices of bin locations the peak structure remains similarly visible (the dip is strongly diluted from the smearing and the binning as discussed in the previous subsections). To quantitatively evaluate the significance of the signal of the resonant

Table 8 Values of the variable R for the sensitivity of the signal for different bin locations for a 10% and 15% smeared distribution and a bin size of 50 GeV

Bin location	R (10% smear)	R (15% smear)
start at 251 GeV (orange)	89.6	87.5
start at 261 GeV (yellow)	85.8	82.6
start at 271 GeV (purple)	87.8	81.6

enhancement we list the values of R for the two plots discussed above in Table 8.

In Table 8 one can observe that the variation in R stays within 5% when we modify the location of the bins. That means that the uncertainties associated to the location of the bin are smaller than the ones associated to the smearing and about the same as for the bin size. Therefore, overall we find that the experimental resolution of the particle detector, which we tried to mimic by smearing the data, has a larger impact on the resonance, and the width and location of the binning has a smaller effect in diluting the resonance.

5.4 Effect of $\text{sign}(\lambda_{hhH} \times \xi_H^t)$

Finally, taking into account the above discussed experimental uncertainties, we analyze the possibility to access experimentally the relative sign of the involved couplings in the resonant diagram. For this analysis we will use the same benchmark point as above, where the effect of an ad-hoc change of $\text{sign}(\lambda_{hhH} \times \xi_H^t)$ has been shown already in the right plot of Fig. 12 and is reproduced for completeness of this analysis in Fig. 24. On this “ideal” result we will apply a smearing and a binning in order to see whether the difference in the peak-dip vs. dip-peak structure, and thus in the $\text{sign}(\lambda_{hhH} \times \xi_H^t)$, persists in the experimental analysis. This will demonstrate whether the access to this parameter is a realistic goal at the HL-LHC.

The invariant mass distribution of the benchmark point is shown in red for the original value of $\lambda_{hhH} = -0.3975$ and

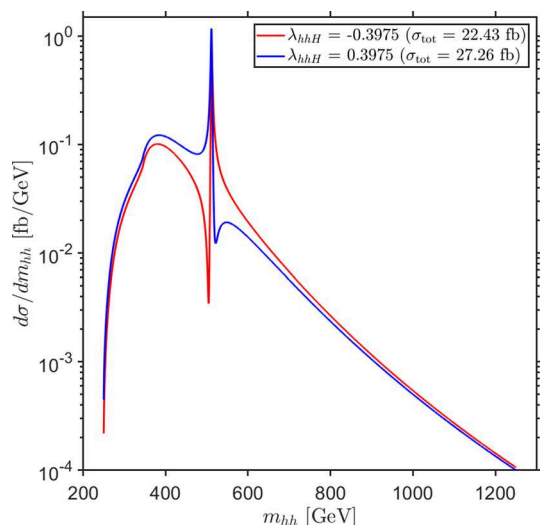


Fig. 24 Invariant mass distributions for different signs of $(\lambda_{hhH} \times \xi_H^t)$ (see the right plot of Fig. 12)

a positive sign of $(\lambda_{hhH} \times \xi_H^t)$, whereas the blue line gives the result for an ad-hoc changed sign of $\lambda_{hhH} = +0.3975$ and a negative sign of $(\lambda_{hhH} \times \xi_H^t)$. Both distributions are normalized to the corresponding value of the total cross section, which is indicated in the legend of Fig. 24. The change in the structure is clearly visible in this plot. We remind that the value of the top Yukawa coefficient in this case was, as obtained from Eq. (16), $\xi_H^t = 0.104 > 0$. Therefore we see that for an overall minus (plus) sign the imprinted structure of the resonance in the m_{hh} spectrum is a peak-dip (dip-peak) one.

We now impose the various experimental uncertainties on the “ideal” result shown in Fig. 24. We start with the application of smearing as presented in Fig. 25. In the left (right) plot a 10% (15%) smearing is applied. The red and blue curves correspond, as before, to the negative and positive sign of λ_{hhH} . The black curves indicate the continuum distribution. One can observe that the blue curve is above (below) the

red one right before (after) the bump. However, the overall structure cannot be resolved once the data is smeared.

The final step is the application of binning on top of a 15% smearing, which is the most realistic experimental set up. The results are shown in Fig. 26. One can conclude that effectively the dip-peak vs. peak-dip structure becomes unresolvable once both smearing and binning is applied.

6 Conclusions

In this work we have analyzed the impact of BSM triple Higgs couplings on the production cross section of two ~ 125 GeV Higgs bosons at the HL-LHC, where the 2HDM has been chosen as an example framework. The first goal was to analyze the impact of λ_{hhh} (with a focus on deviations from its SM value) and λ_{hhH} on the di-Higgs production cross section and in particular to investigate the possibility of experimental sensitivity. In a second step we analyzed the potential sensitivity of the HL-LHC on the BSM THC λ_{hhH} employing the m_{hh} distributions. This sensitivity has been analyzed w.r.t. various experimental uncertainties. While it is crucial to determine all THC's of the Higgs sector realized in nature, no analyses for BSM Higgs-boson couplings at the HL-LHC is available so far. Consequently, here we explore for the first time the potential sensitivity to BSM THC's, as well as corresponding experimental effects at the HL-LHC.

We have chosen several observables that allow us to trace the impact of the THC's. The first one is the Higgs pair production cross section that is affected by the diagrams containing these couplings. Using the code HPAIR we have evaluated the cross sections of di-Higgs production including NLO QCD corrections (in the heavy top limit) in the specific benchmark planes that were selected to represent the various phenomenological situations that can occur in the 2HDM. We have analyzed the numerical impact of the THC's, and in particular the contribution of the heavy Higgs boson in the propagator and its decay width.

Fig. 25 Invariant mass distributions for different signs of $(\lambda_{hhH} \times \xi_H^t)$ with a 10% (left) and 15% (right) smearing applied. The black line shows the continuum distribution

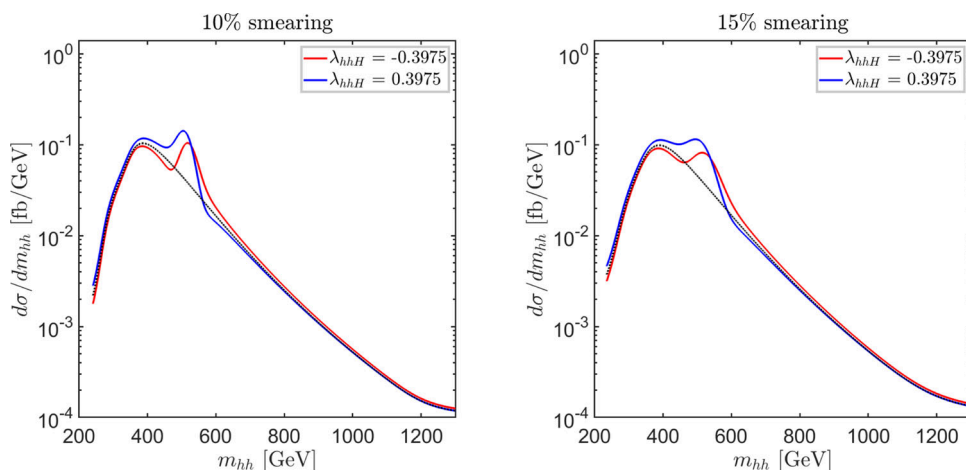
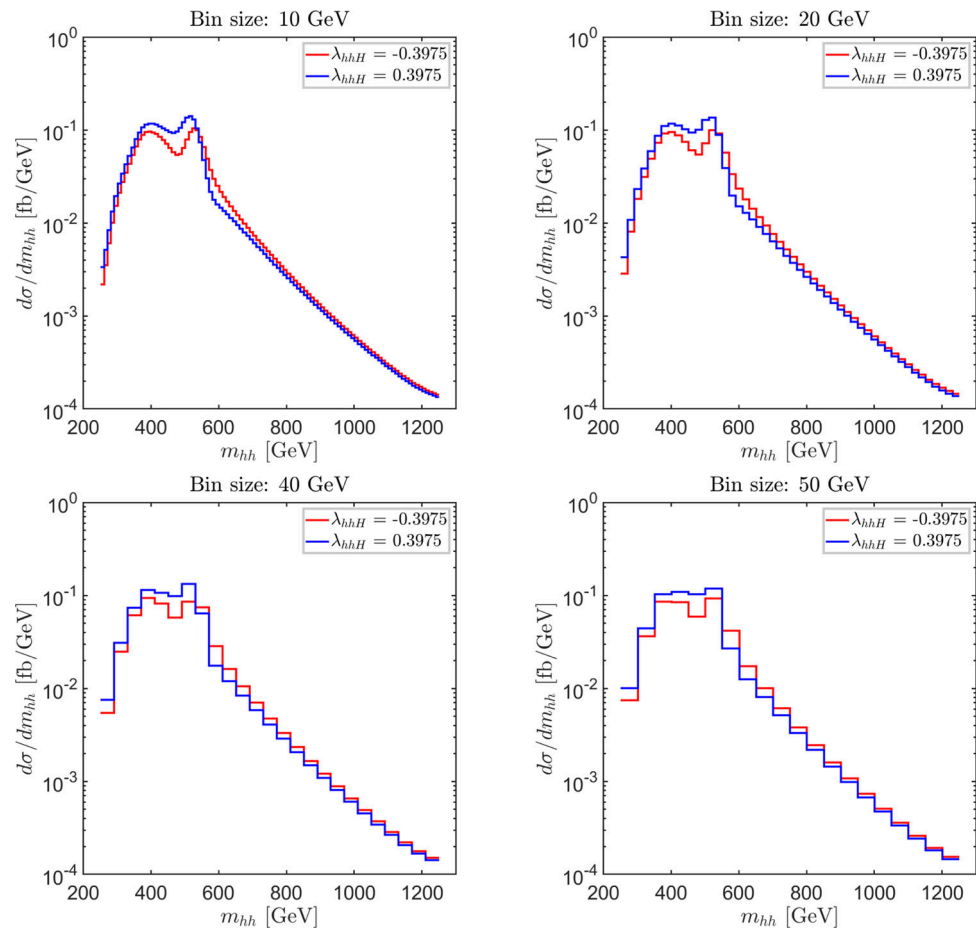


Fig. 26 Invariant mass distributions for different signs of $(\lambda_{hhH} \times \xi_H^t)$ with a 15% smearing applied. Results for different bin sizes: 10 GeV (upper left), 20 GeV (upper right), 40 GeV (lower left) and 50 GeV (lower right)



Differences of the di-Higgs production cross sections can originate from a changed value of λ_{hhH} , as well as from additional “resonant” contributions, given by the s -channel exchange of the heavy \mathcal{CP} -even Higgs boson, H . In the analyzed benchmark planes we have found both types of effects, which can yield a strong enhancement of the di-Higgs production cross section w.r.t. its SM result. Using the projection for the experimental resolution of the di-Higgs production cross section at the HL-LHC we found effects in the few σ range, but also ranging up to 10σ , or higher. While these results indicate that the effect of the resonant s -channel H contribution may be visible, from the cross section alone it is not possible to disentangle the two sources.

In order to gain more direct access to λ_{hhH} we analyzed the invariant di-Higgs mass distributions, $d\sigma/dm_{hh}$ as a function of m_{hh} . To our knowledge, this is the first analysis in this direction. The investigated effects are so far not taken into account in the searches for resonant contributions in the di-Higgs boson searches. Consequently, we expect that our findings support and facilitate the search for BSM Higgs bosons in the resonant di-Higgs measurements. Furthermore, they lay the ground work for the extraction of BSM THC from the di-Higgs searches.

Starting with a toy example we analyzed the interference of the resonant H exchange with the non-resonant (continuum) diagrams. The interference term changes sign for $Q = m_{hh} = m_H$, resulting in a peak-dip (or dip-peak) structure of the m_{hh} distribution (where often in the experimental search for resonant di-Higgs production only a simplified peak structure is assumed). We demonstrated that the interference effect becomes smaller with the total decay width of the H and that the “total width of the effect”, given by the width of the peak at half of its maximum value, increases with increasing Γ_H^{tot} . Furthermore, the structure of the interference (peak-dip vs. dip-peak) depends on the sign of $(\lambda_{hhH} \times \xi_H^t)$, which enters as a prefactor of the interference contribution (ξ_H^t denotes the top Yukawa coupling of the heavy \mathcal{CP} -even Higgs boson).

The effects in the toy example were reproduced for the complete m_{hh} distribution for several points in the before chosen benchmark planes. We demonstrated the dependencies of the size of the interference effects on λ_{hhH} and ξ_H^t for large di-Higgs production cross sections, as well as for selected points closer to the alignment limit ($c_{\beta-\alpha} \sim 0.1$) and further away from the alignment limit ($c_{\beta-\alpha} \sim 0.2$). These results indicate that the HL-LHC may have sensitivity to see effects of the BSM THC λ_{hhH} . As a theoretical

variable quantifying the *relative* sensitivity to λ_{hhH} , the variable R was defined, see Eq. (17). However, it is not meant as a determination of the experimental λ_{hhH} precision that requires a detailed experimental analysis, which is beyond the scope of our paper

In order to further analyze a possible sensitivity, we applied various experimental uncertainties on R . The first one is the smearing due to the detector resolution, which realistically can go down to $\sim 15\%$, but we also analyzed a potential (optimistic) improvement down to 10%. It is found that from the dip-peak structure mostly a bump survives, with a very small reduction due to the dip w.r.t. the unsmeared result. The next effect is the binning of the result, mostly given by the b -jet mass resolution from the reconstruction of the $h \rightarrow b\bar{b}$ decay of one of the Higgs bosons. A realistic value of a 50 GeV bin size was compared to more optimistic sizes down to 10 GeV. While the smearing has a visible effect on R , the binning hardly reduces its value. Similarly, the location of the bin, which is partially arbitrary, has a smaller impact on R once we take into account the finite resolution of the detector (smearing). As a last step we showed that the $\text{sign}(\lambda_{hhH} \times \xi_H^t)$ does not leave any measurable imprint on the m_{hh} distributions, once the experimental uncertainties are taken into account.

We conclude that, depending on the values of the underlying Lagrangian parameters, a sizable resonant H contribution to the di-Higgs production cross section can leave possibly visible effects in the m_{hh} distribution. This would pave the way for a first determination of a BSM THC, a step that is crucial for the reconstruction of the Higgs potential of the underlying BSM model. We leave a detailed analysis in which for parts of the parameter space such a determination will be possible for future work.

Acknowledgements We thank D. Azevedo, M.J. Herrero, J. Schaarschmidt, M. Spira and G. Weiglein for helpful discussions. The work of F.A. and S.H. has received financial support from the grant PID2019-110058GB-C21 funded by MCIN/AEI/10.13039/501100011033 and by “ERDF A way of making Europe”. MEINCOP Spain under contract PID2019-110058GB-C21. and in part by the grant IFT Centro de Excelencia Severo Ochoa CEX2020-001007-S funded by MCIN/AEI/10.13039/501100011033. The work F.A. has furthermore received financial support from the Spanish “Agencia Estatal de Investigación” (AEI) and the EU “Fondo Europeo de Desarrollo Regional” (FEDER) through the project PID2019-108892RB-I00/AEI/10.13039/501100011033, from the European Union’s Horizon 2020 research and innovation programme under the Marie Skłodowska-Curie grant agreement No 674896 and No 860881-HIDDeN; and from the FPU grant with code FPU18/06634. The work of M.M. has been supported by the BMBF-Project 05H21VKCCA. K.R. acknowledges support by the Deutsche Forschungsgemeinschaft (DFG, German Research Foundation) under Germany’s Excellence Strategy – EXC 2121 “Quantum Universe” – 390833306. This work has been partially funded by the Deutsche Forschungsgemeinschaft (DFG, German Research Foundation) – 491245950.

Data Availability Statement This manuscript has no associated data or the data will not be deposited. [Authors’ comment: There is no associated data with the manuscript.]

Open Access This article is licensed under a Creative Commons Attribution 4.0 International License, which permits use, sharing, adaptation, distribution and reproduction in any medium or format, as long as you give appropriate credit to the original author(s) and the source, provide a link to the Creative Commons licence, and indicate if changes were made. The images or other third party material in this article are included in the article’s Creative Commons licence, unless indicated otherwise in a credit line to the material. If material is not included in the article’s Creative Commons licence and your intended use is not permitted by statutory regulation or exceeds the permitted use, you will need to obtain permission directly from the copyright holder. To view a copy of this licence, visit <http://creativecommons.org/licenses/by/4.0/>.

Funded by SCOAP³. SCOAP³ supports the goals of the International Year of Basic Sciences for Sustainable Development.

References

1. G. Aad et al., [ATLAS Collaboration]. Phys. Lett. B **716**, 1 (2012). [arXiv:1207.7214](#) [hep-ex]
2. S. Chatrchyan et al., [CMS Collaboration]. Phys. Lett. B **716**, 30 (2012). [arXiv:1207.7235](#) [hep-ex]
3. G. Aad et al., [ATLAS and CMS Collaborations]. JHEP **1608**, 045 (2016). [arXiv:1606.02266](#) [hep-ex]
4. [ATLAS], ATLAS-CONF-2022-050
5. [CMS], Nature **607**(7917), 60 (2022). [arXiv:2207.00043](#) [hep-ex]
6. H. Abouabid et al., JHEP **09**, 011 (2022). [arXiv:2112.12515](#) [hep-ph]
7. J. de Blas et al., JHEP **01**, 139 (2020). [arXiv:1905.03764](#) [hep-ph]
8. B. Di Micco et al., Rev. Phys. **5**, 100045 (2020). [arXiv:1910.00012](#) [hep-ph]
9. T.D. Lee, Phys. Rev. D **8**, 1226 (1973)
10. J.F. Gunion, H.E. Haber, G.L. Kane, S. Dawson, Front. Phys. **80**, 1–404 (2000). SCIPP-89/13. Erratum: [arXiv:hep-ph/9302272](#)
11. M. Aoki, S. Kanemura, K. Tsumura, K. Yagyu, Phys. Rev. D **80**, 015017 (2009). [arXiv:0902.4665](#) [hep-ph]
12. G.C. Branco, P.M. Ferreira, L. Lavoura, M.N. Rebelo, M. Sher, J.P. Silva, Phys. Rep. **516**, 1 (2012). [arXiv:1106.0034](#) [hep-ph]
13. S.L. Glashow, S. Weinberg, Phys. Rev. D **15**, 1958 (1977)
14. F. Arco, S. Heinemeyer, M.J. Herrero, Eur. Phys. J. C **80**(9), 884 (2020). [arXiv:2005.10576](#) [hep-ph]
15. F. Arco, S. Heinemeyer, M.J. Herrero, Eur. Phys. J. C **82**(6), 536 (2022). [arXiv:2203.12684](#) [hep-ph]
16. P. Bambade et al. [arXiv:1903.01629](#) [hep-ex]
17. P. N. Burrows et al., [CLICdp and CLIC], [arXiv:1812.06018](#) [physics.acc-ph]
18. A. Djouadi, W. Kilian, M. Mühlleitner, P.M. Zerwas, Eur. Phys. J. C **10**, 27–43 (1999). [arXiv:hep-ph/9903229](#) [hep-ph]
19. H. Abramowicz et al., Eur. Phys. J. C **77**(7), 475 (2017). [arXiv:1608.07538](#) [hep-ex]
20. J. Strube, [ILC Physics and Detector Study], Nucl. Part. Phys. Proc. **273–275**, 2463–2465 (2016)
21. P. Roloff et al., [CLICdp]. Eur. Phys. J. C **80**(11), 1010 (2020). [arXiv:1901.05897](#) [hep-ex]
22. F. Arco, S. Heinemeyer, M.J. Herrero, Eur. Phys. J. C **81**(10), 913 (2021). [arXiv:2106.11105](#) [hep-ph]
23. T. Kon, T. Nagura, T. Ueda, K. Yagyu, Phys. Rev. D **99**(9), 095027 (2019). [arXiv:1812.09843](#) [hep-ph]
24. N. Sonmez, JHEP **10**, 083 (2018). [arXiv:1806.08963](#) [hep-ph]

25. A. Djouadi, W. Kilian, M. Mühlleitner, P.M. Zerwas, Eur. Phys. J. C **10**, 45 (1999). [arXiv:hep-ph/9904287](#)
26. P. Basler, M. Mühlleitner, J. Wittbrodt, JHEP **03**, 061 (2018). [arXiv:1711.04097](#) [hep-ph]
27. P. Basler, M. Mühlleitner, J. Müller, JHEP **05**, 016 (2020). [arXiv:1912.10477](#) [hep-ph]
28. J. Baglio et al., JHEP **04**, 151 (2013). [arXiv:1212.5581](#) [hep-ph]
29. S. Dawson, S. Dittmaier, M. Spira, Phys. Rev. D **58**, 115012 (1998). [arXiv:hep-ph/9805244](#)
30. R. Grober, M. Mühlleitner, M. Spira, Nucl. Phys. B **925**, 1 (2017). [arXiv:1705.05314](#) [hep-ph]
31. J. Ren, R.Q. Xiao, M. Zhou, Y. Fang, H.J. He, W. Yao, JHEP **06**, 090 (2018). [https://doi.org/10.1007/JHEP06\(2018\)090](https://doi.org/10.1007/JHEP06(2018)090). [arXiv:1706.05980](#) [hep-ph]
32. M.E. Peskin, T. Takeuchi, Phys. Rev. Lett. **65**, 964 (1990)
33. M.E. Peskin, T. Takeuchi, Phys. Rev. D **46**, 381 (1992)
34. T. Aaltonen et al., [CDF], Science **376**(6589), 170–176 (2022)
35. H. Song, W. Su, M. Zhang, JHEP **10**, 048 (2022). [arXiv:2204.05085](#) [hep-ph]
36. H. Bahl, J. Braathen, G. Weiglein, Phys. Lett. B **833**, 137295 (2022). [arXiv:2204.05269](#) [hep-ph]
37. K.S. Babu, S. Jana, P.K. Vishnu, Phys. Rev. Lett. **129**(12), 12 (2022). [arXiv:2204.05303](#) [hep-ph]
38. R. L. Workman et al., [Particle Data Group], PTEP **2022**, 083C01 (2022)
39. F. Arco, S. Heinemeyer, M.J. Herrero, Phys. Lett. B **835**, 137548 (2022). [arXiv:2207.13501](#) [hep-ph]
40. P. Bechtle, O. Brein, S. Heinemeyer, G. Weiglein, K.E. Williams, Comput. Phys. Commun. **181**, 138 (2010). [arXiv:0811.4169](#) [hep-ph]
41. P. Bechtle, O. Brein, S. Heinemeyer, G. Weiglein, K.E. Williams, Comput. Phys. Commun. **182**, 2605 (2011). [arXiv:1102.1898](#) [hep-ph]
42. P. Bechtle, O. Brein, S. Heinemeyer, O. Stål, T. Stefaniak, G. Weiglein, K.E. Williams, Eur. Phys. J. C **74**(3), 2693 (2014). [arXiv:1311.0055](#) [hep-ph]
43. P. Bechtle, S. Heinemeyer, O. Stål, T. Stefaniak, G. Weiglein, Eur. Phys. J. C **75**, 421 (2015). [arXiv:1507.06706](#) [hep-ph]
44. P. Bechtle, D. Dercks, S. Heinemeyer, T. Klingl, T. Stefaniak, G. Weiglein, J. Wittbrodt, Eur. Phys. J. C **80**(12), 1211 (2020). [arXiv:2006.06007](#) [hep-ph]
45. H. Bahl, T. Biekötter, S. Heinemeyer, C. Li, S. Paasch, G. Weiglein, J. Wittbrodt, [arXiv:2210.09332](#) [hep-ph]
46. D. Eriksson, J. Rathsmann, O. Stål, Comput. Phys. Commun. **181**, 189 (2010). [arXiv:0902.0851](#) [hep-ph]
47. A. Djoudi, J. Kalinowski, M. Spira, Comput. Phys. Commun. **108**, 56 (1998). [arXiv:hep-ph/9704448](#)
48. A. Djoudi, J. Kalinowski, M. Muehlleitner, M. Spira, Comput. Phys. Commun. **238**, 214 (2019). [arXiv:1801.09506](#) [hep-ph]
49. R. Harlander et al., [arXiv:1312.5571](#) [hep-ph]
50. P. Bechtle, S. Heinemeyer, O. Stål, T. Stefaniak, G. Weiglein, Eur. Phys. J. C **74**(2), 2711 (2014). [arXiv:1305.1933](#) [hep-ph]
51. P. Bechtle, S. Heinemeyer, O. Stål, T. Stefaniak, G. Weiglein, JHEP **1411**, 039 (2014). [arXiv:1403.1582](#) [hep-ph]
52. P. Bechtle, S. Heinemeyer, T. Klingl, T. Stefaniak, G. Weiglein, J. Wittbrodt, Eur. Phys. J. C **81**(2), 145 (2021). [arXiv:2012.09197](#) [hep-ph]
53. T. Enomoto, R. Watanabe, JHEP **1605**, 002 (2016). [arXiv:1511.05066](#) [hep-ph]
54. A. Arbey, F. Mahmoudi, O. Stål, T. Stefaniak, Eur. Phys. J. C **78**(3), 182 (2018). [arXiv:1706.07414](#) [hep-ph]
55. F. Mahmoudi, Comput. Phys. Commun. **180**, 1579 (2009). [arXiv:0808.3144](#) [hep-ph]
56. F. Mahmoudi, Comput. Phys. Commun. **180**, 1718–1719 (2009)
57. T. Plehn, M. Spira, P.M. Zerwas, Nucl. Phys. B **479**, 46–64 (1996) (Erratum: Nucl. Phys. B **531**, 655–655 (1998)). [arXiv:hep-ph/9603205](#)
58. S. Borowka et al., Phys. Rev. Lett. **117**(1) (2016), 012001 (Erratum-ibid. **117**(7) (2016), 079901). [arXiv:1604.06447](#) [hep-ph]
59. S. Borowka et al., JHEP **1610**, 107 (2016). [arXiv:1608.04798](#) [hep-ph]
60. J. Baglio et al., Eur. Phys. J. C **79**, 459 (2019). [arXiv:1811.05692](#) [hep-ph]
61. J. Baglio et al., JHEP **04**, 181 (2020). [arXiv:2003.03227](#) [hep-ph]
62. J. Baglio et al., Phys. Rev. D **103**(5), 056002 (2021). [arXiv:2008.11626](#) [hep-ph]
63. D. de Florian, J. Mazzitelli, Phys. Rev. Lett. **111**, 201801 (2013). [arXiv:1309.6594](#) [hep-ph]
64. J. Grigo et al., Nucl. Phys. B **888**, 17 (2014). [arXiv:1408.2422](#) [hep-ph]
65. D.Y. Shao et al., JHEP **07**, 169 (2013). [arXiv:1301.1245](#) [hep-ph]
66. D. de Florian, J. Mazzitelli, JHEP **09**, 053 (2015). [arXiv:1505.07122](#) [hep-ph]
67. P. Banerjee et al., JHEP **11**, 130 (2018). [arXiv:1809.05388](#) [hep-ph]
68. L. Chen et al., Phys. Lett. B **803**, 135292 (2020). [arXiv:1909.06808](#) [hep-ph]
69. L. Chen et al., JHEP **03**, 072 (2020). [arXiv:1912.13001](#) [hep-ph]
70. A.H. Ajath, H. Shao, [arXiv:2209.03914](#) [hep-ph]
71. M. Mühlleitner, J. Schlenk, M. Spira, JHEP **10**, 185 (2022). [arXiv:2207.02524](#) [hep-ph]
72. J. Davies et al., JHEP **08**, 259 (2022). [arXiv:2207.02587](#) [hep-ph]
73. J. Baglio, F. Campanario, S. Glaus, M. Mühlleitner, J. Ronca, M. Spira, [arXiv:2303.05409](#) [hep-ph]
74. M. Capozzi, G. Heinrich, JHEP **03**, 091 (2020). [arXiv:1908.08923](#) [hep-ph]
75. A. Buckley et al., Eur. Phys. J. C **75**, 132 (2015). [arXiv:1412.7420](#) [hep-ph]
76. S. Dulat et al., Phys. Rev. D **93**(3), 033006 (2016). [arXiv:1506.07443](#) [hep-ph]
77. J.R. Andersen, S. Badger, L. Barze, J. Bellm, F.U. Bernlochner, A. Buckley, J. Butterworth, N. Chanon, M. Chiesa, A. Cooper-Sarkar, et al., [arXiv:1405.1067](#) [hep-ph]
78. M. Cepeda et al., CERN Yellow Rep. Monogr. **7**, 221–584 (2019). [arXiv:1902.00134](#) [hep-ph]
79. J. List, priv. commun
80. A.M. Sirunyan et al., [CMS], JHEP **04** (2020), 171 (Erratum: JHEP **03** (2022), 187)